JGR Planets

RESEARCH ARTICLE
10.1029/2019JE005936

**Key Points:**
- The sound velocity and density of liquid Fe-Ni-S (17 and 30 at% S) and Fe-Ni-Si (29 and 38 at% Si) were measured up to 14 GPa
- Based on the obtained elastic properties, estimated S contents in the core are 4.6 wt% S for Mercury and 32.4 wt% S for Mars
- Difference in sound velocity between the Fe-Ni-S and Fe-Ni-Si core is large enough to be detected in the core compositions of Mars and Moon

**Correspondence to:**
H. Terasaki,
terasaki@ess.sci.osaka-u.ac.jp

**Citation:**
Terasaki, H., Rivoldini, A., Shimoyama, Y., Nishida, K., Urakawa, S., Maki, M., et al (2019). Pressure and composition effects on sound velocity and density of core-forming liquids: Implication to core compositions of terrestrial planets. *Journal of Geophysical Research: Planets*, *124*, 2272–2293. https://doi.org/10.1029/2019JE005936

Received 5 FEB 2019
Accepted 7 AUG 2019
Accepted article online 13 AUG 2019
Published online 28 AUG 2019

**Author Contributions:**
**Conceptualization:** Hidenori Terasaki
**Formal analysis:** Hidenori Terasaki
**Investigation:** Hidenori Terasaki
**Methodology:** Keisuke Nishida
**Writing - original draft:** Hidenori Terasaki, Keisuke Nishida

# Pressure and Composition Effects on Sound Velocity and Density of Core-Forming Liquids: Implication to Core Compositions of Terrestrial Planets

**Hidenori Terasaki[1], Attilio Rivoldini[2], Yuta Shimoyama[1], Keisuke Nishida[3], Satoru Urakawa[4], Mayumi Maki[1], Fuyuka Kurokawa[1], Yusaku Takubo[1], Yuki Shibazaki[5,6], Tatsuya Sakamaki[7], Akihiko Machida[8], Yuji Higo[9], Kentaro Uesugi[9], Akihisa Takeuchi[9], Tetsu Watanuki[8], and Tadashi Kondo[1]**

[1]Department of Earth and Space Science, Osaka University, Osaka, Japan, [2]Royal Observatory of Belgium, Brussels, Belgium, [3]Department of Earth and Planetary Science, The University of Tokyo, Tokyo, Japan, [4]Department of Earth Science, Okayama University, Okayama, Japan, [5]Frontier Research Institute for Interdisciplinary Sciences, Tohoku University, Sendai, Japan, [6]Now at International Center for Young Scientists, National Institute for Materials Science, Ibaraki, Japan, [7]Department of Earth Science, Tohoku University, Sendai, Japan, [8]Synchrotron Radiation Research Center, National Institutes for Quantum and Radiological Science and Technology, Hyogo, Japan, [9]Japan Synchrotron Radiation Research Institute, Hyogo, Japan

**Abstract** A compositional variety of planetary cores provides insight into their core/mantle evolution and chemistry in the early solar system. To infer core composition from geophysical data, a precise knowledge of elastic properties of core-forming materials is of prime importance. Here, we measure the sound velocity and density of liquid Fe-Ni-S (17 and 30 at% S) and Fe-Ni-Si (29 and 38 at% Si) at high pressures and report the effects of pressure and composition on these properties. Our data show that the addition of sulfur to iron substantially reduces the sound velocity of the alloy and the bulk modulus in the conditions of this study, while adding silicon to iron increases its sound velocity but has almost no effect on the bulk modulus. Based on the obtained elastic properties combined with geodesy data, S or Si content in the core is estimated to 4.6 wt% S or 10.5 wt% Si for Mercury, 9.8 wt% S or 18.3 wt% Si for the Moon, and 32.4 wt% S or 30.3 wt% Si for Mars. In these core compositions, differences in sound velocity profiles between an Fe-Ni-S and Fe-Ni-Si core in Mercury are small, whereas for Mars and the Moon, the differences are substantially larger and could be detected by upcoming seismic sounding missions to those bodies.

**Plain Language Summary** To estimate core compositions of terrestrial planets using geophysical data with high-pressure physical property of core-forming materials, we measure the sound velocity and density of liquid Fe-Ni-S and Fe-Ni-Si at high pressures. The effect of S and Si on elastic properties are quite different in the present conditions. Based on the obtained physical properties combined with geodesy data, S or Si content in the core of Mercury, Moon, and Mercury are estimated. In these core compositions, differences in sound velocity profiles between an Fe-Ni-S and Fe-Ni-Si core in Mars and the Moon are substantially large and could be detected by upcoming seismic sounding mission to Mars.

## 1. Introduction

Mercury, Mars, and Earth's moon (the Moon) are reported, from geophysical observations, to have a liquid core (Margot et al., 2007; Williams et al., 2001; Yoder et al., 2003). These planetary bodies are thought to have a core that mainly consists of Fe-5 ~ 10 wt% Ni and of some fractions of light elements (LEs; S, Si, O, C, and H; Dreibus & Wänke, 1985; Smith et al., 2012; Steenstra et al., 2016). Thus, the core is one of the major reservoirs of LEs in planetary body. Knowledge of the composition of the core of terrestrial planets is important not only for inferring the internal structure and thermal state of a planet, which strongly influence the core/mantle dynamics and their evolution, but also for understanding the distribution of LE in the solar nebula of the inner solar system (e.g., Rubie et al., 2015). To obtain constraints on the core composition, sound velocity and density of liquid Fe-alloys measured under planetary core conditions are indispensable information together with geodesy and geophysical data, such as mean density, moment of inertia, tidal Love number, and seismic wave velocity.

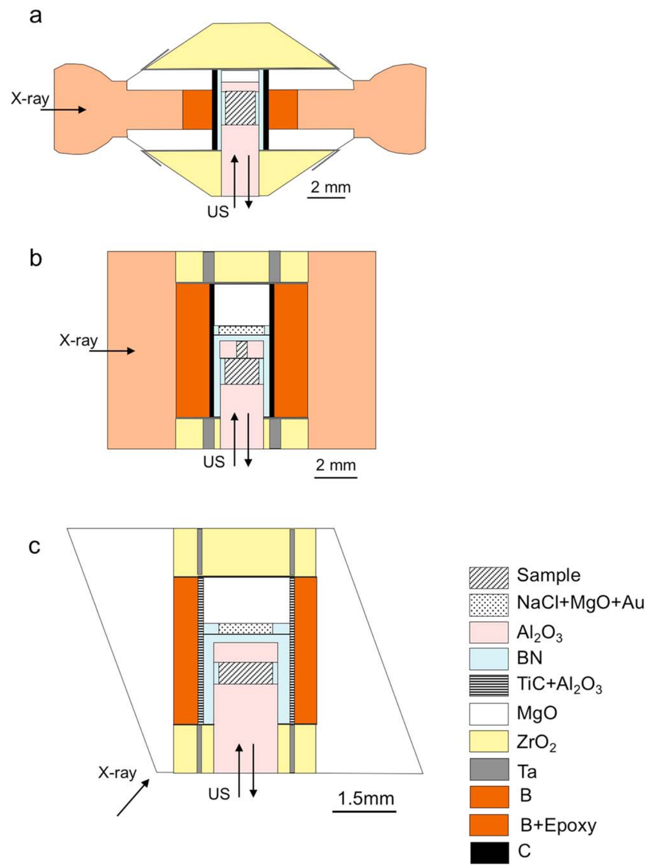


**Figure 1.** Schematic illustrations of used cell assemblies. A monochromatic X-ray passes horizontally through the center of the cell. The ultrasonic signal (US) comes from the bottomside of the cell as shown by arrows. (a) Cupped-type cell used for $P < 1$ GPa at BL20XU. (b) Cell assembly of cubic-type multianvil press used for $1 < P < 5$ GPa at BL22XU. (c) Cell assembly of Kawai-type multianvil press used for $P > 5$ GPa at BL04B1.

S and Si are known to be the major candidates as the LEs in planetary cores, as they have high solar abundance (Palme & Jones, 2005) and are present in primordial meteorites. Fe-Ni-S is widely found in chondrites and iron meteorites (Mittlefehldt et al., 1998), and Fe-Ni-Si is found in enstatite chondrites (Brearley & Jones, 1998), which are one of the candidate building blocks for the Earth (Javoy et al., 2010), Mars (Sanloup et al., 1999), and Mercury (Wasson, 1989). Because the solubility of S and Si in liquid Fe strongly depends on the oxygen fugacity conditions in the planetary interiors (Malavergne et al., 2010), identifying the core LEs also provides information about the redox environment inside the planet.

Recently, the compressional wave velocities ($V_P$) of liquid Fe-Ni, Fe-S, and Fe-C have been measured in static high-pressure experiments. These results show that S, C, and Ni reduce the $V_P$ of liquid Fe at pressures below 10 GPa (Jing et al., 2014; Kuwabara et al., 2016; Nishida et al., 2013, 2016; Shimoyama et al., 2016), while S and C increase the $V_P$ of liquid Fe above 10 GPa (Kawaguchi et al., 2017; Nakajima et al., 2015). To explain these trends, a possible change in the structure and electronic properties of liquid Fe-S is thought to occur at around 10 GPa (Kawaguchi et al., 2017). However, these two opposing trends were obtained by different methods, that is, ultrasonic method below 10 GPa and inelastic X-ray scattering (IXS) method above 10 GPa. To ascertain the exact elastic behavior, $V_P$ data should be measured using the same method in wide pressure range, especially below and above 10 GPa. In addition, $V_P$ measurements at high-pressure for liquid Fe-Ni-Si, an important candidate for the core material, has never been reported.

In this paper, we investigate the effects of pressure, temperature, and LEs (S and Si) on the sound velocity and density of potential core-forming liquids (Fe-Ni-S and Fe-Ni-Si) by using the ultrasonic pulse-echo overlap method and the X-ray absorption method. Then, the core compositions of Mercury, the Moon, and Mars are estimated based on the obtained elastic properties, in conjunction with geodesy data, and hence we propose the seismic wave velocity and density profiles of these bodies.

## 2. Methods

### 2.1. Sample Compositions

The sample compositions used were $Fe_{73}Ni_{10}S_{17}$ in at% (S = 10.5 wt%) and $Fe_{60}Ni_{10}S_{30}$ (S = 19.6 wt%) for liquid Fe-Ni-S, and $Fe_{61}Ni_{10}Si_{29}$ (Si = 16.9 wt%) and $Fe_{52}Ni_{10}Si_{38}$ (Si = 23.4 wt%) for liquid Fe-Ni-Si. These were composed of a mixture of powdered Fe, Ni (both were 99.99%) and FeS (99.9%) or FeSi (99.9%). The pelleted sample was enclosed in a hexagonal-BN cylinder. The top and bottom of the sample pellet were sandwiched by a mirror-polished single crystal sapphire buffer rod and a backing plate (Figure 1).

### 2.2. High-Pressure Experiments

High pressure was generated using three different high-pressure apparatuses generating different pressure ranges. The sound velocity was measured using the ultrasonic pulse-echo overlapping method. The density was measured using the X-ray absorption method based on the Beer-Lambert law or using the X-ray computed tomography (CT) measurement. For the measurements below 1 GPa, an 80-ton portable uniaxial press (Urakawa et al., 2010) was used combined with X-ray computed-tomography (CT) measurements (Kuwabara et al., 2016) at the BL20XU beamline, SPring-8 synchrotron radiation facility in Japan. High pressure was generated using opposing cupped WC anvils (diameter of the center cup was 12 mm) with a ringed groove. The cell assembly was a toroidal type as shown in Figure 1a. For the measurements from 1 to 5 GPa, we used a 180-ton cubic-type multianvil press at BL22XU beamline, SPring-8 (Shimoyama et al., 2016). The truncated edge length of the tungsten carbide anvil was 6 mm. We used two different sample diameters in

10.1029/2019JE005936

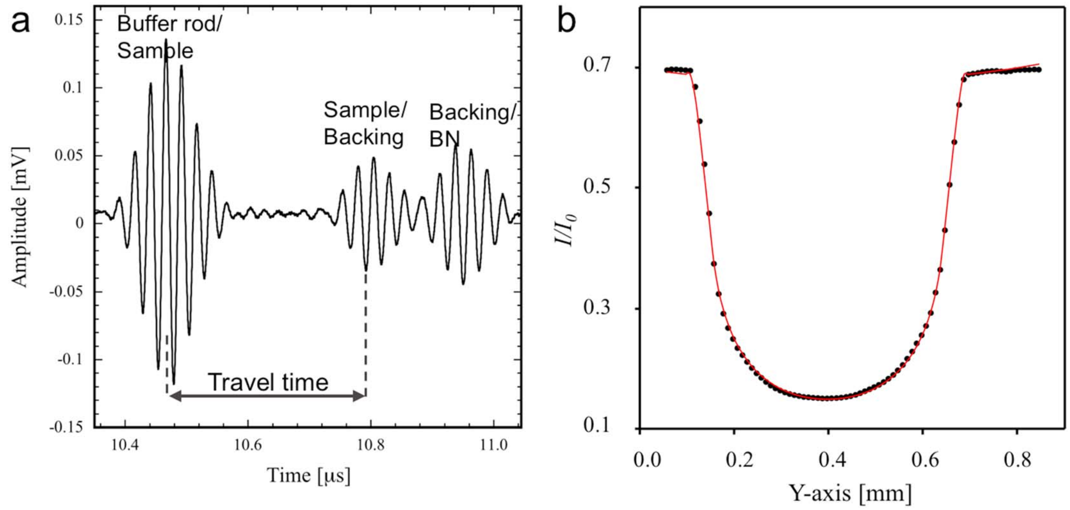


**Figure 2.** (a) Echo signal of the liquid $Fe_{73}Ni_{10}S_{17}$ sample obtained at 2.8 GPa and 1600 K. The three sinusoidal signals correspond to echoes at the Fe-Ni-S sample front (buffer rod/sample), sample back (sample/backing plate), and backing plate/BN, respectively (see the assembly in Figure 1b). The time between the sample front and the back corresponds to the two-way travel time in the sample, as indicated by an arrow. (b) X-ray absorption profile of the liquid $Fe_{73}Ni_{10}S_{17}$ at 2.8 GPa and 1600 K as a function of position on a horizontal axis ($Y$) perpendicular to the X-ray. Black circles and red curve denote raw data and fitted curve using the Beer-Lambert law, respectively.

the same cell (Figure 1b). The initial diameter of the sample for sound velocity measurement was 1.5 mm to obtain a clear echo signal from the sample interfaces and that for density measurement was 0.5 mm to obtain appropriate X-ray absorption contrast between the sample and surrounding materials. For measurements above 5 GPa, a 1,500-ton Kawai-type multianvil press was used at BL04B1 beamline, SPring-8 (Nishida et al., 2013). The truncated edge length of the 2nd stage tungsten carbide anvils was 5 mm. The cell assemblies used in this study are shown in Figure 1c.

Monochromatized X-rays (37.7 keV at BL20XU, 35 keV at BL22XU, and 51 keV at BL04B1), which were tuned by Si (111) or Si (311) double-crystal monochromators, were used (Shobu et al., 2007; Suzuki et al., 2004). The energies of the X-rays were optimized from the sample size to obtain appropriate X-ray absorption contrasts. The X-ray radiography image was obtained using a complementary metal-oxide semiconductor camera (ORCA-flash 4.0, Hamamatsu Photonics K. K., Japan) with an Yttrium Aluminium Garnet (YAG) scintillator.

The X-ray diffraction (XRD) spectra of the sample and pressure markers (MgO and hexagonal-BN for experiments at $P < 5$ GPa; MgO, NaCl and Au for experiments at $P > 5$ GPa) were collected using a complementary metal-oxide semiconductor flat panel detector (C7942-CA/C7942CK-12, Hamamatsu Photonics K. K.) to determine density of solid phases, and the experimental pressures and temperatures, respectively. Melting of the samples was identified by the disappearance of the XRD peaks and the appearance of a diffuse scattering signal. The experimental pressures and temperatures were obtained from the lattice volumes of a pair of pressure markers combined with their equations of state (MgO: Tange et al., 2009; hexagonal-BN: Wakabayashi & Funamori, 2015; NaCl: Matsui, 2009; Au: Tsuchiya, 2003). Difference in pressure and temperature between sample and pressure marker in the cell (Figure 1c) were checked by placing the pressure marker in the sample capsule instead of the sample. Both difference in pressure and temperature between the sample and pressure marker becomes to be quite small at higher temperature above 800 K ($\Delta P < 0.5$ GPa and $\Delta T < 60$ K).

### 2.3. Sound Velocity Measurement

Compressional wave velocity ($V_P$) was measured using the ultrasonic pulse-echo overlap method (Higo et al., 2009). A 10° Y-cut $LiNbO_3$ transducer was attached to the backside of the anvil to generate and receive compressional wave acoustic signals. Input electric signals of sine waves with frequencies of 35–45 MHz were generated using a waveform generator (AWG2021/AFG3251C/AWG710B, Tektronix Inc.).

**Table 1**
*Experimental Conditions and Measured Sound Velocity and Density of Liquid Fe-Ni-S*

| Run no. | $P$ (GPa)[a] | $P$ error[b] | T (K) | $V_P$ (m/s) | $V_P$ error | $\rho$ (g/cm$^3$) | $\rho$ error |
|---|---|---|---|---|---|---|---|
| $Fe_{73}Ni_{10}S_{17}$ | | | | | | | |
| B268 | 2.8 | 0.2 | 1600 | 3,530 | 20 | 6.18 | 0.04 |
| | 2.8 | 0.2 | 1720 | 3,540 | 20 | 6.19 | 0.05 |
| B261 | 3.2 | 0.1 | 1900 | 3,650 | 20 | 6.13 | 0.03 |
| | 3.2 | 0.2 | 1970 | 3,700 | 10 | | |
| | 3.2 | 0.2 | 2040 | 3,720 | 20 | 5.99 | 0.03 |
| | 3.1 | 0.1 | 2060 | 3,690 | 30 | | |
| | 3.0 | 0.1 | 2080 | 3,690 | 30 | 6.05 | 0.03 |
| B274 | 3.8 | 0.0 | 1680 | 4,040 | 80 | 6.37 | 0.05 |
| | 3.8 | 0.1 | 1760 | 3,990 | 60 | | |
| | 3.9 | 0.2 | 1840 | 3,990 | 60 | | |
| | 3.9 | 0.2 | 1890 | 3,930 | 50 | | |
| | 3.9 | 0.3 | 1940 | 3,930 | 50 | 6.35 | 0.05 |
| S3069 | 7.5 | 0.5 | 1830 | 4,370 | 140 | | |
| | 7.2 | 0.5 | 2040 | 4,380 | 200 | | |
| | 7.0 | 0.5 | 2150 | 4,310 | 280 | | |
| | 7.0 | 0.5 | 2200 | 4,240 | 320 | | |
| S2991 | 10.0 | 0.1 | 1510 | 4,780 | 90 | | |
| | 9.8 | 0.1 | 1570 | 4,830 | 100 | | |
| S3067 | 10.4 | 0.6 | 2100 | 4,890 | 290 | | |
| | 10.5 | 0.6 | 2250 | 4,830 | 260 | | |
| | 10.5 | 0.6 | 2250 | 4,660 | 250 | | |
| S3090 | 13.9 | 0.1 | 1610 | 4,950 | 180 | | |
| $Fe_{60}Ni_{10}S_{30}$ | | | | | | | |
| B277 | 2.4 | 0.2 | 1660 | 3,120 | 10 | 5.65 | 0.02 |
| | 2.4 | 0.3 | 1740 | 3,130 | 10 | | |
| | 2.5 | 0.3 | 1810 | 3,140 | 10 | 5.51 | 0.02 |
| | 2.3 | 0.5 | 1910 | 3,140 | 10 | | |
| B263 | 3.0 | 0.1 | 1620 | 3,240 | 20 | | |
| | 3.1 | 0.1 | 1690 | 3,280 | 20 | 5.71 | 0.02 |
| | 3.1 | 0.1 | 1690 | 3,290 | 20 | 5.71 | 0.02 |
| | 3.1 | 0.1 | 1700 | 3,300 | 20 | | |
| | 3.1 | 0.2 | 1890 | 3,310 | 20 | 5.58 | 0.02 |
| | 3.1 | 0.2 | 1890 | 3,310 | 10 | | |
| | 3.0 | 0.3 | 1960 | 3,270 | 20 | | |
| | 3.0 | 0.3 | 1960 | 3,270 | 20 | | |
| B275 | 3.4 | 0.0 | 1450 | | | 5.70 | 0.03 |
| | 3.4 | 0.0 | 1560 | 3,360 | 40 | | |
| | 3.6 | 0.0 | 1640 | 3,390 | 40 | | |
| | 3.8 | 0.0 | 1710 | 3,400 | 30 | | |
| S3070 | 7.3 | 0.7 | 1330 | 3,650 | 290 | | |
| | 7.3 | 0.7 | 1410 | 3,700 | 260 | | |
| | 7.4 | 0.6 | 1500 | 3,660 | 240 | | |
| | 7.4 | 0.5 | 1580 | 3,730 | 260 | | |
| | 7.5 | 0.4 | 1670 | 3,650 | 270 | | |
| S3068 | 10.4 | 0.1 | 1490 | 4,110 | 250 | | |
| | 10.3 | 0.1 | 1520 | 4,160 | 250 | | |
| | 10.3 | 0.1 | 1520 | 4,110 | 220 | | |
| | 10.1 | 0.0 | 1580 | 4,160 | 220 | | |
| | 9.8 | 0.0 | 1650 | 4,220 | 200 | | |
| | 9.7 | 0.1 | 1700 | 4,090 | 200 | | |
| S3091 | 12.6 | 0.1 | 1240 | 4,310 | 120 | | |
| | 12.4 | 0.1 | 1340 | 4,340 | 110 | | |

[a]Used pressure marker pairs were BN+MgO: B268, 261, 274, 277, 263, 275; NaCl+MgO: S2991, 3067, 3090, 3070, 3068, 3091; NaCl+Au: S3069, 3067. [b]Pressure errors were derived from errors in lattice volumes of pressure markers.

**Table 2**
*Experimental Conditions and Measured Sound Velocity and Density of Liquid Fe-Ni-Si*

| Run no. | $P$ (GPa)[a] | $P$ error[b] | $T$ (K) | $V_P$ (m/s) | $V_P$ error | $\rho$ (g/cm$^3$) | $\rho$ error |
|---|---|---|---|---|---|---|---|
| *$Fe_{61}Ni_{10}Si_{29}$* | | | | | | | |
| HPT26 | 0.3 | 0.04 | 2070 | 3,990 | 50 | | |
| HPT24 | 0.4 | 0.02 | 1590 | 4,070 | 30 | | |
| | 0.3 | 0.02 | 1680 | 3,960 | 30 | | |
| B250 | 2.5 | 0.05 | 1680 | | | 6.37 | 0.03 |
| | 2.5 | 0.05 | 1730 | 4,360 | 90 | | |
| | 2.5 | 0.05 | 1780 | 4,360 | 80 | 6.23 | 0.03 |
| | 2.5 | 0.00 | 1880 | 4,360 | 60 | | |
| | 2.5 | 0.00 | 1970 | 4,290 | 80 | 6.17 | 0.04 |
| B247 | 3.3 | 0.09 | 1950 | | | 6.24 | 0.04 |
| | 3.3 | 0.35 | 2020 | 4,510 | 170 | | |
| | 3.3 | 0.22 | 2060 | 4,400 | 170 | | |
| B251 | 4.2 | 0.05 | 1790 | | | 6.32 | 0.06 |
| | 4.4 | 0.10 | 1840 | | | 6.34 | 0.06 |
| | 4.5 | 0.10 | 1880 | 4,600 | 40 | 6.32 | 0.06 |
| | 4.4 | 0.20 | 1890 | 4,610 | 50 | | |
| | 4.3 | 0.29 | 1910 | | | 6.29 | 0.06 |
| *$Fe_{52}Ni_{10}Si_{38}$* | | | | | | | |
| HPT23 | 0.5 | 0.12 | 1770 | 4,140 | 90 | | |
| | 0.4 | 0.04 | 1910 | 4,180 | 330 | | |
| B282 | 2.1 | 0.13 | 1630 | 4,530 | 30 | | |
| | 2.1 | 0.14 | 1690 | 4,500 | 30 | | |
| | 2.1 | 0.14 | 1740 | 4,470 | 30 | | |
| B260 | 2.9 | 0.10 | 1830 | | | 5.87 | 0.03 |
| | 2.8 | 0.16 | 1860 | 4,450 | 60 | | |
| | 2.7 | 0.22 | 1880 | | | | |
| | 2.8 | 0.13 | 2090 | 4,430 | 60 | 5.60 | 0.03 |
| B285 | 3.9 | 0.23 | 1970 | 4,540 | 20 | | |
| S3143 | 9.7 | 0.60 | 1690 | 5,150 | 100 | | |
| | 10.0 | 0.54 | 1560 | 5,330 | 110 | | |
| | 9.9 | 0.57 | 1630 | 5,220 | 110 | | |
| | 9.5 | 0.63 | 1780 | 5,160 | 140 | | |
| | 9.3 | 0.67 | 1870 | 5,080 | 110 | | |
| | 9.1 | 0.71 | 1960 | 5,100 | 140 | | |
| | 8.9 | 0.75 | 2060 | 5,030 | 100 | | |
| S3140 | 11.8 | 0.15 | 1900 | 5,350 | 140 | | |
| | 11.9 | 0.15 | 1820 | 5,380 | 140 | | |
| | 11.7 | 0.15 | 1980 | 5,300 | 140 | | |
| | 11.5 | 0.15 | 2050 | 5,280 | 150 | | |

*Note*. Used pressure marker pairs were BN+MgO: B250, 247, 251, 282, 260, 285; NaCl+MgO: S3143, 3140; BN[3]: HPT26, 24, 23.
[a]$P$ was estimated from EoS of BN and $T$ was calibrated from separate run as described in Terasaki et al. (2019). [b]Pressure errors were derived from errors in lattice volumes of pressure markers.

The echo signals from the sample were detected using a high-resolution digital oscilloscope (DPO5054/DPO7104, Tektronix Inc.) with a sampling rate of $5 \times 10^9$ or $1 \times 10^{10}$ points/s. The signal travel time in the sample was obtained from the time difference in the echo signals between the near and far sides of the sample interfaces. The length of the sample was measured from the X-ray radiography image (pixel size = 2.5–3.0 μm). The sample thickness ranges 330–745 μm below 10 GPa and 240–460 μm above 10 GPa. The $V_P$ was calculated from the measured travel time and sample length. Details of travel time and sample length analyses are described elsewhere (Kono et al., 2012). A typical example of an echo signal from the sample interface is shown in Figure 2a. The error in $V_P$, listed in Tables 1 and 2, was derived mainly from estimated errors in sample length determination, which was caused mainly by clearness of image contrast and brightness and also by variation in sample length and from the travel time uncertainty caused by overlapping echo signals.

### 2.4. Density Measurement

The density was measured from the X-ray absorption method (Katayama, 1996) based on the Beer-Lambert law or from volume measurement using X-ray CT. For X-ray absorption method, a monochromatized X-ray was collimated to 50 × 50-μm size and introduced to the sample. Intensities of incident ($I_0$) and transmitted ($I$) X-rays, through the sample, were measured using two ion chambers located upstream and downstream of the press, respectively. The X-ray absorption ($I/I_0$) profile of the sample was obtained by scanning the press perpendicular to the X-ray direction with a 10-μm step. A typical example of an X-ray absorption profile of a liquid sample is shown in Figure 2b. The density ($\rho$) of the sample was obtained by fitting the X-ray absorption profile with the Beer-Lambert law,

$$I/I_0 = \exp(-\mu_s \rho_s t_s - \mu_e \rho_e t_e), \tag{1}$$

where $\mu$ and $t$ denote mass absorption coefficient and thickness of X-ray absorbers, respectively. Subscripts $s$ and $e$ represent sample and surrounding materials, respectively. The $\mu$ of the sample, $\mu_s$, can be determined from the solid sample density measured using XRD and its X-ray absorption profile. Then, the sample density, $\rho_s$, and thickness, $t_s$, were deduced by fitting the profile using equation (1). Details of this procedure were reported in previous study (Shimoyama et al., 2016). The density error, listed in Tables 1 and 2, was mainly derived from fitting error for the X-ray absorption profile using equation (1). For X-ray CT measurement, the volume of the sample was obtained from in situ 3-D image measured using X-ray CT. Details of the X-ray CT are given in Appendix A.

## 3. Results

The experimental conditions and obtained results are given in Tables 1 and 2. The compressional wave velocities ($V_P$) of liquid Fe-Ni-S ($Fe_{73}Ni_{10}S_{17}$ and $Fe_{60}Ni_{10}S_{30}$) and liquid Fe-Ni-Si ($Fe_{61}Ni_{10}Si_{29}$ and $Fe_{52}Ni_{10}Si_{38}$) are shown in Figures 3a and 3b. The $V_P$ of liquid Fe-Ni-S increases nonlinearly and that of liquid Fe-Ni-Si increases more monotonously with pressure. The $V_P$ of liquid $Fe_{73}Ni_{10}S_{17}$ is similar to that of liquid $Fe_{80}S_{20}$ (Nishida et al., 2016; open diamonds in Figure 3a), suggesting that the effect of Ni on the $V_P$ of liquid Fe-S is small. The $V_P$ of liquid Fe-Ni-S is less sensitive to temperature (see Table 1), which is

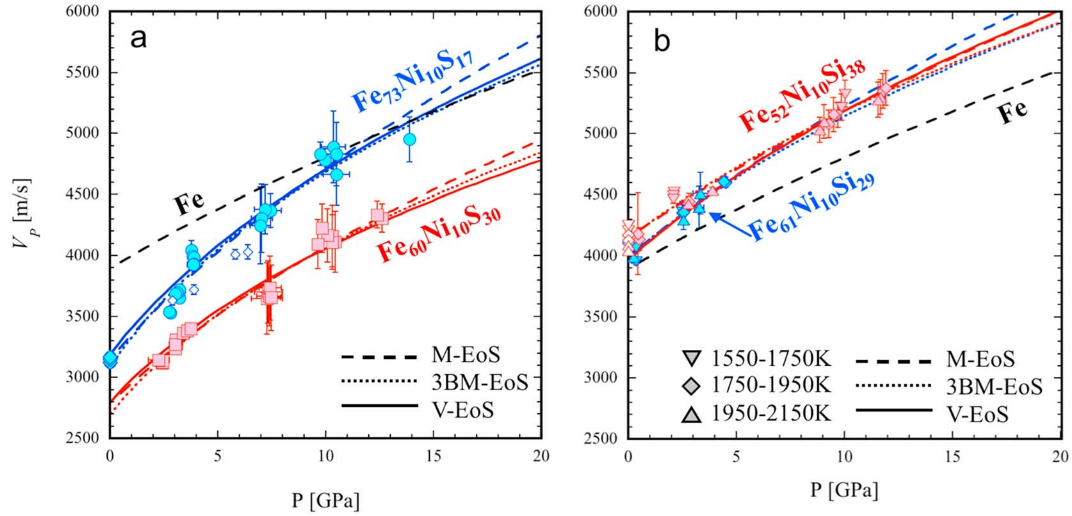


**Figure 3.** The effect of pressure on $V_P$. Dashed, dotted, and solid curves represent fittings using Murnaghan, third-order Brich-Murnaghan, and Vinet EoS, respectively. The $V_P$ of liquid Fe are shown by black dashed (Jing et al., 2014). (a) Liquid Fe-Ni-S. Blue circles and red squares denote the $V_P$ of $Fe_{73}Ni_{10}S_{17}$ and $Fe_{60}Ni_{10}S_{30}$, respectively. Open diamonds indicate reported $V_P$ of liquid $Fe_{80}S_{20}$ (Nishida et al., 2016). As the effect of $T$ on $V_P$ is minor (see text), we plotted $V_P$ at all $T$ conditions. Data at ambient pressure are taken from Nasch et al. (1997). (b) Liquid Fe-Ni-Si. Blue and red symbols denote the $V_P$ of $Fe_{61}Ni_{10}Si_{29}$ and $Fe_{52}Ni_{10}Si_{38}$, respectively. Different symbol shapes represent different temperatures as shown in the legend. Data at ambient pressure are taken from Williams et al. (2015).

consistent with previous results for liquid Fe-S (Jing et al., 2014; Nishida et al., 2013). On the other hand, the $V_P$ of liquid Fe-Ni-Si decreases slightly with increasing temperature with $dV_P/dT$ of −0.42 to −0.57 $ms^{-1}\cdot K^{-1}$ (see Table 2). The $dV_P/dT$ found in this study is in agreement with that measured at ambient pressure (−0.36 to −0.52 $ms^{-1}\cdot K^{-1}$; Williams et al., 2015).

The $V_P$ of a liquid is expressed using density ($\rho$) and adiabatic bulk modulus ($K_S$) as follows:

**Table 3**
*Adiabatic Elastic Properties*

| Composition | EoS[a] | $T_0$ (K) | $K_{S0}$ (GPa) | $K_{S0}$ error | $K'_S$ | $K'_S$ error | $\rho_0$ [g/cm$^3$] | $\rho_0$ error | $\alpha_0$ ($10^{-5}$/K) | $\alpha_0$ error | $dK_S/dT$ | $dK_S/dT$ error | $\gamma_0$ (fix) | $\delta_{S0}$[b] |
|---|---|---|---|---|---|---|---|---|---|---|---|---|---|---|
| $Fe_{73}Ni_{10}S_{17}$ | M | 1650 | 58.8 | 1.6 | 8.7 | 0.3 | 5.91 | 0.02 | | | | | | |
| | 3BM | 1650 | 56.2 | 3.5 | 11.2 | 0.4 | 5.91 | 0.02 | | | | | | |
| | V | 1650 | 55.2 | 3.2 | 10.5 | 0.7 | 5.91 | 0.02 | 10.1 | 1.8 | −0.01 | 0.001 | 2.30 | 1.8 |
| $Fe_{60}Ni_{10}S_{30}$ | M | 1650 | 40.8 | 1.0 | 6.0 | 0.2 | 5.21 | 0.02 | | | | | | |
| | 3BM | 1650 | 38.1 | 1.8 | 7.4 | 0.2 | 5.21 | 0.02 | | | | | | |
| | V | 1650 | 37.1 | 1.9 | 7.8 | 0.4 | 5.21 | 0.02 | 11.0 | (fix) | −0.004 | 0.002 | 2.30 | 1.0 |
| $Fe_{61}Ni_{10}Si_{29}$ | M | 1650 | 98.5 | 1.5 | 8.3 | 0.6 | 6.15 | 0.03 | | | | | | |
| | 3BM | 1650 | 97.9 | 2.3 | 8.8 | 0.5 | 6.15 | 0.03 | | | | | | |
| | V | 1650 | 96.5 | 2.6 | 9.3 | 0.9 | 6.15 | 0.03 | 9.5 | 3.3 | −0.015 | 0.010 | 1.73 | 1.6 |
| $Fe_{52}Ni_{10}Si_{38}$ | M | 1550 | 101.9 | 1.3 | 7.0 | 0.2 | 5.95 | 0.07 | | | | | | |
| | 3BM | 1550 | 102.1 | 1.1 | 7.8 | 0.1 | 5.95 | 0.07 | | | | | | |
| | V | 1550 | 108.4 | 4.1 | 7.1 | 0.5 | 5.95 | 0.07 | 20.4 | 4.0 | −0.049 | 0.014 | 1.73 | 2.2 |
| $Fe_{90}Ni_{10}$ | M[c] | 1900 | 103.0 | 2.0 | 5.7 | 0.8 | 6.97 | | | | | | | |
| | 3BM[c] | 1900 | 103.1 | 1.7 | 6.0 | 0.1 | 6.97 | | | | | | | |
| Fe | M[d] | 1673 | 105.0 | 2.0 | 6.7 | 1.0 | 6.91 | | | | | | | |
| | 3BM[e] | 1811 | 109.7 | 0.7 | 4.7 | 0.0 | 7.02 | | | | | | | |

*Note.* $\delta_S$ is given from $\alpha$, $K_S$, and $dK_S/dT$ using $\delta_S = -(1/\alpha K_S)(dK_S/dT)_P$.
[a]Abbreviations: M: Murnaghan EoS, 3BM: third-order Birch-Murnaghan EoS, V: Vinet EoS. [b]Note that $\delta_S = -(1/\alpha K_S)(dK_S/dT)_P$. [c]Kuwabara et al. (2016). [d]Jing et al. (2014). [e]Anderson & Ahrens (1994).

**Table 4**
*Isothermal Elastic Properties*

| Composition | EoS[a] | $T_0$ (K) | $K_{T0}$ (GPa) | $K_{T0}$ error | $K'_T$ | $K'_T$ error | $\rho_0$ (g/cm$^3$) | $\rho_0$ error | $\alpha_0$ ($10^{-5}$/K) | $\alpha_0$ error | $dK_T/dT$ | $dK_T/dT$ error | $\gamma_0$ (fix) | $\delta_{T0}$[b] |
|---|---|---|---|---|---|---|---|---|---|---|---|---|---|---|
| $Fe_{73}Ni_{10}S_{17}$ | 3BM | 1650 | 40.7 | 1.4 | 10.6 | 0.3 | 5.91 | 0.02 | 10.0 | 1.8 | −0.014 | 0.004 | 2.30 | 3.4 |
| | V | 1650 | 38.5 | 3.1 | 10.0 | 0.6 | 5.91 | 0.02 | 10.0 | 1.8 | −0.014 | 0.004 | 2.30 | 3.6 |
| $Fe_{60}Ni_{10}S_{30}$ | 3BM | 1650 | 27.7 | 1.0 | 7.8 | 0.2 | 5.24 | 0.02 | 11.0 | (fix) | −0.018 | 0.006 | 2.30 | 5.9 |
| | V | 1650 | 28.0 | 2.0 | 7.4 | 0.4 | 5.24 | 0.02 | 11.0 | (fix) | −0.018 | 0.006 | 2.30 | 5.8 |
| $Fe_{61}Ni_{10}Si_{29}$ | 3BM | 1650 | 76.8 | 1.2 | 8.3 | 0.4 | 6.15 | 0.03 | 9.6 | 3.4 | −0.022 | 0.011 | 1.73 | 3.0 |
| | V | 1650 | 75.9 | 6.1 | 8.6 | 1.0 | 6.15 | 0.03 | 9.6 | 3.4 | −0.022 | 0.011 | 1.73 | 3.0 |
| $Fe_{52}Ni_{10}Si_{38}$ | 3BM | 1550 | 69.0 | 0.1 | 7.5 | 0.1 | 5.94 | 0.07 | 19.7 | 3.5 | −0.050 | 0.010 | 1.73 | 3.7 |
| | V | 1550 | 70.0 | 4.0 | 7.1 | 0.4 | 5.94 | 0.07 | 19.7 | 3.5 | −0.050 | 0.010 | 1.73 | 3.6 |

[a]Abbreviations: M: Murnaghan EoS, 3BM: third-order Birch-Murnaghan EoS, V: Vinet EoS. [b]Note that $\delta_T = -(1/\alpha K_T)(dK_T/dT)_P$. Note that $\alpha_0$ and $dK_T/dT$ of 3BM were used from those of Vinet EoS.

$$V_P(P,T) = \sqrt{\frac{K_S(P,T)}{\rho(P,T)}} \tag{2}$$

where $\rho$ and $K_S$ are expressed as function of pressure ($P$) and temperature ($T$) using equations of state (EoS). For the effect of pressure on the $V_P$, previous studies have assumed either a linear dependence of $V_P$ on $P$ (Nishida et al., 2013) or a Murnaghan EoS (Jing et al., 2014), where $K_S$ is a linear function of $P$. In this study, we considered three types of EoS—Murnaghan EoS (M), third-order Birch-Murnaghan EoS (3BM), and Vinet EoS (V)—to assess the pressure dependence of $V_P$. The 3BM EoS is widely used for compression behavior of solid materials and the V EoS is reported to provide a more accurate description of compressional behavior for highly compressible materials, such as liquids (Cohen et al., 2000). The expressions for three EoS are given in Appendix B. The elastic properties ($K_0$ and $K'$) have been obtained by fitting

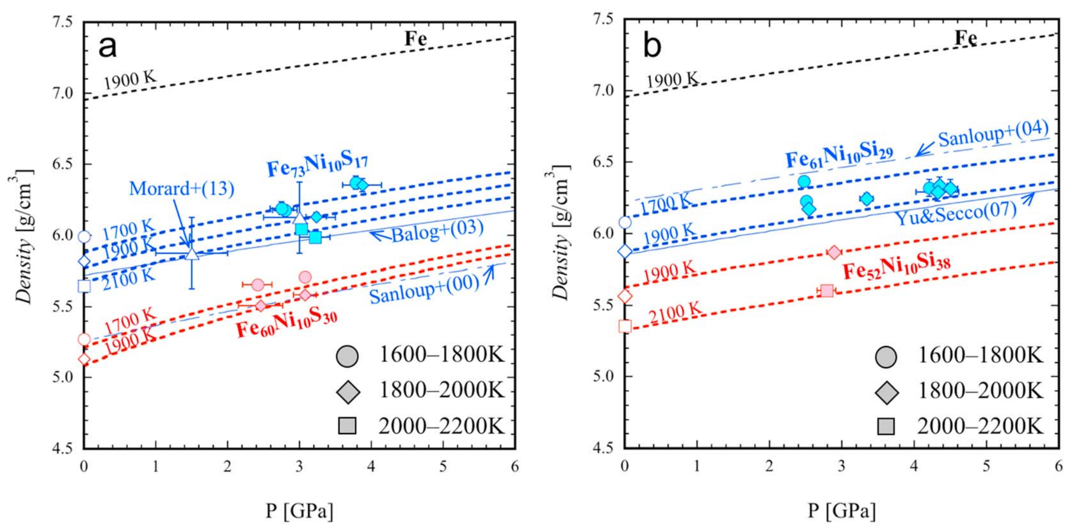


**Figure 4.** The effect of pressure on $\rho$. Different symbol shapes represent different temperatures as shown in the legend. Dashed curves indicate the calculated density from isothermal 3BM-EoS at different temperatures. The $\rho$ of liquid Fe is shown by black dashed curve (Anderson & Ahrens, 1994). (a) Liquid Fe-Ni-S. Blue and red symbols denote the $\rho$ of $Fe_{73}Ni_{10}S_{17}$ and $Fe_{60}Ni_{10}S_{30}$, respectively. The $\rho_0$ (density at ambient pressure) were taken from the data of Nagamori (1969). Open triangles indicate the $\rho$ of liquid $Fe_{77.1}S_{22.9}$ (14.6 wt%S) at 1860 K reported by Morard, Garbarino, et al. (2013), Morard, Siebert, et al. (2013). Blue solid and dash-dotted curves respectively represent the $\rho$ of liquid $Fe_{84}S_{16}$ (10 wt%S) at 1700 K reported by Balog et al. (2003) and that by Sanloup et al. (2000). (b) Liquid Fe-Ni-Si. Blue and red symbols denote the $\rho$ of $Fe_{61}Ni_{10}Si_{29}$ and $Fe_{52}Ni_{10}Si_{38}$, respectively. The $\rho_0$ were taken from data of Kawai et al. (1974). Blue solid and dash-dotted curves, respectively, represent the $\rho$ of liquid $Fe_{71}Si_{29}$ (17 wt%Si) at 1800 K reported by Yu and Secco (2008) and by Sanloup et al. (2004).

**Table 5**
*EoS Parameters of End Members*

| Parameter | Fe[c] | FeS[d] | FeSi[e] |
|---|---|---|---|
| $\rho_0$ (g/cm$^3$) | 7.019 | 3.725 | 5.103 |
| $K_{T0}$ (GPa) | 85.1 | 18.3 | 69.0 |
| $K_T'$ | 5.8 | 5.8 | 7.4 |
| d$K$/d$T$ (GPa/K) | −0.035 | — | −0.042 |
| $\delta_T$ [a] | — | 10.10 | 3.47 |
| $\alpha_0$ [$10^{-5}$ K$^{-1}$] | —[b] | 12.88 | 17.54 |
| $\gamma_0$ | 1.4 | 1.4 | 1.6 |
| $T_0$ [K] | 1811 | 1650 | 1723 |

[a]$\delta_T$ is Anderson-Gruneisen parameter defined as $\alpha/\alpha_0 = (\rho_0/\rho)^{\delta T}$. [b]$\rho_0(T)$ (g/cm$^3$) = $[(1.3105 \times 10^{-5})(T - T_0) + 0.14247]^{-1}$. [c]Anderson & Ahrens (1994). [d]Nagamori (1969); Kaiura & Toguri (1979); Nishida et al. (2016); Antonangeli et al. (2015). [e]Kawai et al. (1074); Dumay & Cramb (1995); Yu & Secco (2008); Williams et al. (2015).

the $V_P$ and/or $\rho$ data of Fe-Ni-S and Fe-Ni-Si liquids using the EoSs (equations (B1)–(B7) in Appendix B) with equation (2). Isentropic and isothermal elastic properties in Tables 3 and 4 are obtained independently from isentropic and isothermal fittings, respectively. Details of the isothermal and isentropic fittings are given in Appendix B. The errors of elastic properties are derived from fitting error, in which the errors of $V_P$ and density data are also taken into account. The errors of all the obtained elastic properties are listed in Tables 3 and 4.

The measured $V_P$ and the fitted EoS are shown in Figure 3. The 3BM- and V-EoS reproduce the $V_P$ data well and show a similar trend within the pressure range of the experiments (Figures 3a and 3b). On the contrary, the M-EoS does not reproduce the $V_P$ data adequately especially for liquid Fe-Ni-S. The calculated $V_P$ using the M-EoS deviates from the measured $V_P$ data and from the calculated $V_P$ using the 3BM- or V-EoS at pressures greater than 10 GPa (Figure 3a). This can be attributed to the assumption in the M-EoS that $K_S$ is a simple linear function of $P$ [see equation (B2)]. Thus, the 3BM- or V-EoS fits are more appropriate to express the pressure dependence of $V_P$ especially for compressible liquids such as Fe-Ni-S. These EoS can accurately link the $V_P$ data obtained at lower pressures from ultrasonic method with that obtained at higher pressures from the IXS method. Although a discontinuous change in d$V_P$/d$P$ or in elastic properties at around 10 GPa was suggested by Kawaguchi et al. (2017) who adopted the M-EoS fit, there is no clear evidence of this discontinuous change in our data when we use the 3BM- or V-EoS fits. Thus, we do not consider such discontinuity in this study. The obtained $K_{S0}$ and $K'_S$ of this study from the 3BM- and V-EoS fits are almost comparable (Tables 3 and 4).

The densities of liquid Fe-Ni-S and Fe-Ni-Si are plotted as a function of pressure in Figures 4a and 4b together with previously reported densities. The compression curve of liquid $Fe_{73}Ni_{10}S_{17}$ in this study agrees with the density reported at 1.8 and 3 GPa (Morard, Garbarino, et al., 2013; Morard, Siebert, et al., 2013) and with the density at ambient pressure extrapolated from data by Nagamori (1969). The density of liquid $Fe_{61}Ni_{10}Si_{29}$ in this study is located between the compression curves of previous studies (Sanloup et al., 2004; Yu & Secco, 2008). Calculated compression curves using $V_P$ and $K_{S0} - K'_S$ data with equation (2) are drawn in Figure 4. They show an excellent agreement with the density measured by X-ray absorption method. This agreement demonstrates the self-consistency of our experiments in which $V_P$ and $\rho$ were measured independently.

## 4. Discussion

### 4.1. The Effect of LEs on the Elastic Properties

The effect of LE on the elastic properties differs significantly depending on alloying LE. Addition of S reduces the $K_{S0}$ of liquid Fe (Anderson & Ahrens, 1994) or Fe-Ni (Kuwabara et al., 2016) from $K_{S0}(Fe_{90}Ni_{10})$ = 103 GPa at 1900 K to $K_{S0}(Fe_{60}Ni_{10}S_{30})$ = 39 GPa at 1650 K, suggesting that the liquid becomes more compressible by adding S even taking into account the different temperature condition. The pressure derivative of the $V_P$ (d$V_P$/d$P$) for liquid Fe-Ni-S is larger than those of liquid Fe and Fe-Ni. These elastic features indicate that the $V_P$ of liquid Fe-Ni-S is lower than that of liquid Fe at lower pressures, while it increases rapidly with pressure to be higher than that of liquid Fe at higher pressures (Figure 3a). On the other hand, addition of Si has little

**Table 6**
*Parameters for Equation (5)*

| | Fe-S system | | Fe-Si system | |
|---|---|---|---|---|
| Parameter | $W_{V(\mathrm{Fe})}$ | $W_{V(\mathrm{FeS})}$ | $W_{V(\mathrm{Fe})}$ | $W_{V(\mathrm{FeSi})}$ |
| $a_i$ | −7.469 ± 0.591 | −0.011 ± 0.512 | −1.679 ± 0.599 | −0.405 ± 0.319 |
| $b_i$ | 1.172 ± 0.338 | 0.875 ± 0.287 | 0 | 0 |

*Note*. The parameters in this table depend on the EoS of Fe (Anderson & Ahrens, 1994; end member) and should only be used with this EoS.

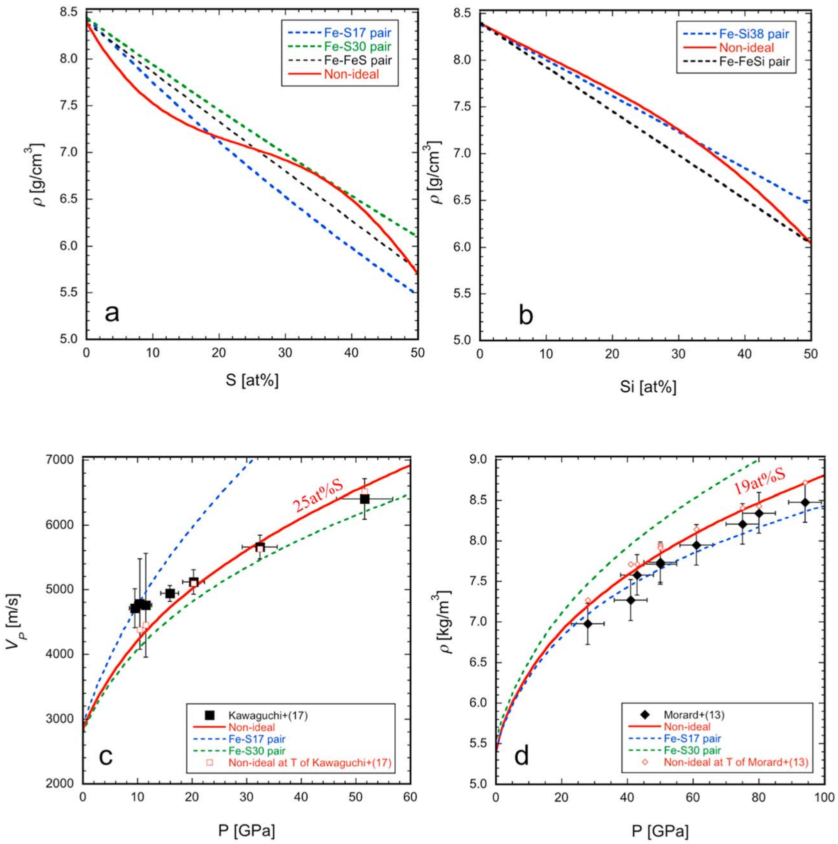


**Figure 5.** Comparison of mixing models. (a) Density of Fe-Ni-S liquid as a function of S concentration at 25 GPa and 1900 K. The blue, green, and black dashed curves represent ideal solution between Fe-$Fe_{73}Ni_{10}S_{17}$ (labeled as Fe-S17), Fe-$Fe_{60}Ni_{10}S_{30}$ (as Fe-S30), and Fe-FeS (labeled as Fe-FeS), respectively. The solid red curve represents the nonideal Fe-FeS solution model of this study. (b) Density of Fe-Ni-Si as a function of Si concentration at 25 GPa and 1900 K. The dashed blue and black curves represent ideal solution between Fe-$Fe_{52}Ni_{10}Si_{38}$ (labeled as Fe-Si38), and Fe-FeSi (labeled as Fe-FeSi), respectively. The solid red curve represents the nonideal Fe-FeSi solution model of this study. (c) $V_P$ plot as a function of pressure. Calculated $V_P$ of liquid Fe-Ni-S from ideal and nonideal mixing models at 1811 K are shown by dashed blue (Fe-S17) and green (Fe-S30) curves and solid red curve, respectively. Black squares represent $V_P$ data of $Fe_{46.5}Ni_{28.5}S_{25}$ of Kawaguchi et al. (2017; the composition at 15.9 GPa was $Fe_{63}Ni_{12}S_{25}$). Red open squares indicate the calculated $V_P$ at the temperature of Kawaguchi et al. (2017). (d) The $\rho$ plot as a function of pressure. Calculated $\rho$ of liquid Fe-Ni-S from ideal and nonideal mixing models at 2300 K are respectively shown by dashed blue or green curves and solid red curve. Black diamonds represent $\rho$ data of $Fe_{76.4}Ni_{4.4}S_{19.2}$ of Morard, Siebert, et al. (2013). Red open triangles indicate the calculated $\rho$ at the temperature of Morard, Siebert, et al. (2013).

influence on the $K_{S0}$ and $K'_S$ of liquid Fe and Fe-Ni but reduces the density (Table 3). As a result, Si increases the $V_P$ of liquid Fe-Ni only moderately (Figure 3b). Differences in the elastic properties of liquid Fe-Ni-S and Fe-Ni-Si can be well explained by a difference in the local structure of the liquid. S strongly modifies the local structure of liquid Fe, and the poorly ordered structure of liquid Fe-S (Sanloup et al., 2002) induces a large effect on the bulk modulus. In contrast, because Si does not affect the local ordering and the local structure of liquid Fe-Si is similar to that of liquid Fe (Sanloup et al., 2002), Si has only a minor effect on the bulk modulus.

### 4.2. Mixing Models

In the next step, we need to understand accurate mixing behaviors of liquid Fe-Ni-S and Fe-Ni-Si under pressure for modeling the planetary cores. In previous studies on planetary core modeling, ideal mixing behavior has been assumed to obtain the core thermoelastic properties as a function of LE content. However, the nonideality of the Fe-S and the Fe-Ni-Si systems are suggested from phase relations and density measured at ambient and moderate pressures (Buono & Walker, 2011; Kawai et al., 1974;

Nagamori, 1969; Nishida et al., 2008; Williams et al., 2015), and ab initio calculations at the Earth's core conditions (Alfè et al., 2003). Thus, we examine the effect of different mixing models (ideal and nonideal mixing) on density and $V_P$ for Fe-Ni-S and Fe-Ni-Si liquids in order to assess which model can best summarize the present data.

In a binary mixing model (end member components 1 and 2), the molar volume of the solution mixture ($V$) is generally given as

$$V = (1-x_2)V_1 + x_2V_2 + V_{\mathrm{ex}} \tag{3}$$

where $V_1$ and $V_2$ denote molar volumes of end members 1 and 2 and $x_2$ is a molar fraction of end member 2. $V_{\mathrm{ex}}$ is the excess molar volume (for ideal-mixing case, $V_{\mathrm{ex}} = 0$). For the ideal mixing, we consider the following end members: (1) Fe and $Fe_{73}Ni_{10}S_{17}$ or Fe and $Fe_{60}Ni_{10}S_{30}$ for the Fe-Ni-S and (2) Fe and $Fe_{52}Ni_{10}Si_{38}$ for the Fe-Ni-Si. The expressions for the thermoelastic properties in an ideal mixing model are described elsewhere (Rivoldini et al., 2011).

For the nonideal mixing model, an asymmetric Margules formulation (e.g., Buono & Walker, 2011) is adopted. Solution end menbers are set to Fe and FeS for the Fe-S system and Fe and FeSi for the Fe-Si. We assume that the effect of Ni on the mixing can be approximated to that of Fe. The $V_1$ and $V_2$ at high pressures and high temperatures are calculated using Vinet EoS with the EoS parameters of the end members listed in Table 5. For the excess molar volume $V_{\mathrm{ex}}$, we have used an asymmetric Margules formulation (Buono & Walker, 2011) written as

$$V_{\mathrm{ex}} = x_2\,(1-x_2)(x_2W_{\mathrm{V1}} + (1-x_2)W_{\mathrm{V2}}) \tag{4}$$

where $W_{\mathrm{V1}}$ and $W_{\mathrm{V2}}$ are the volume interaction (or Margules) parameters for end members 1 and 2, respectively. The interaction parameters have been obtained by fitting the $V_P$ and $\rho$ data of this study ($Fe_{73}Ni_{10}S_{17}$ and $Fe_{60}Ni_{10}S_{30}$ data for the Fe-Ni-S and $Fe_{61}Ni_{10}Si_{29}$ and $Fe_{52}Ni_{10}Si_{38}$ data for the Fe-Ni-Si) to equations (3) and (4). It is found that the measured $V_P$ and $\rho$ data of this study can be represented correctly with interaction parameters of the following form

$$W_{\mathrm{Vi}} = a_i + b_i \log(3/2 + P) \tag{5}$$

where $P$ is pressure in GPa and the $a_{\mathrm{i}}$ and $b_{\mathrm{i}}$ are constants. These constants for end members are given in Table 6. The Grüneisen parameter ($\gamma$) of the solution can be calculated from the isobaric heat capacity of the solution; $C_P = (1-x_2)\,C_{\mathrm{P1}} + x_2\,C_{\mathrm{P2}}$ (from equation 6 of Buono & Walker, 2011) and by using the thermodynamic identities $\gamma = \frac{\alpha K_S V}{C_P}$ and $K_{\mathrm{S}} = (1 + \alpha\gamma\,T)K_T$. Then, from the $\gamma$ of the solution, $K_S$ and $V_P = (K_S/\rho)^{1/2}$ of the solution can be computed.

Calculated densities from ideal and nonideal mixing models are plotted in Figures 5a and 5b at the condition of 25 GPa and 1900 K, an example condition which is near the Martian core-mantle boundary (CMB). For Fe-Ni-S liquid, the $\rho$ of the nonideal mixing model decreases effectively with S than that of ideal mixing models at S < 17 at% (10.5 wt%) and it is bracketed by that of the two ideal mixing (Fe-S17 and Fe-S30) models at S > 17 at% (Figure 5a). For Fe-Ni-Si liquid, density from nonideal mixing is almost consistent with that from ideal mixing in Fe-rich side (up to Si < 30 at%), but it tends to differ in Si-rich side (Si > 30 at%; Figure 5b). Therefore, nonideal mixing behavior is necessary to be considered both for Fe-Ni-S and Fe-Ni-Si systems in order to estimate the elastic properties of Fe-alloys with various S and Si contents. When we extrapolate the $V_P$ and $\rho$ to higher pressures relevant for large planetary cores using both the ideal and nonideal mixing models, the nonideal mixing model well supports recently reported high-pressure data of $V_P$ (Kawaguchi et al., 2017; Figure 5c) and $\rho$ (Morard, Siebert, et al., 2013; Figure 5d). This suggests that the nonideal mixing model combined with Vinet EoS using measured elastic data of this study can accurately link between elastic data obtained at lower pressures and those obtained at higher pressures. This is important when we consider the planetary core which pressure ranges from moderate to high pressures, such as Mercury's core (5–40 GPa) and Martian core (20–40 GPa).

## 5. Implication to Planetary Cores

Here, we model the planetary cores using the thermoelastic properties of liquid Fe-Ni-S and Fe-Ni-Si alloys to constrain the composition of the cores of Mercury, the Moon, and Mars. To compute the thermo-elastic

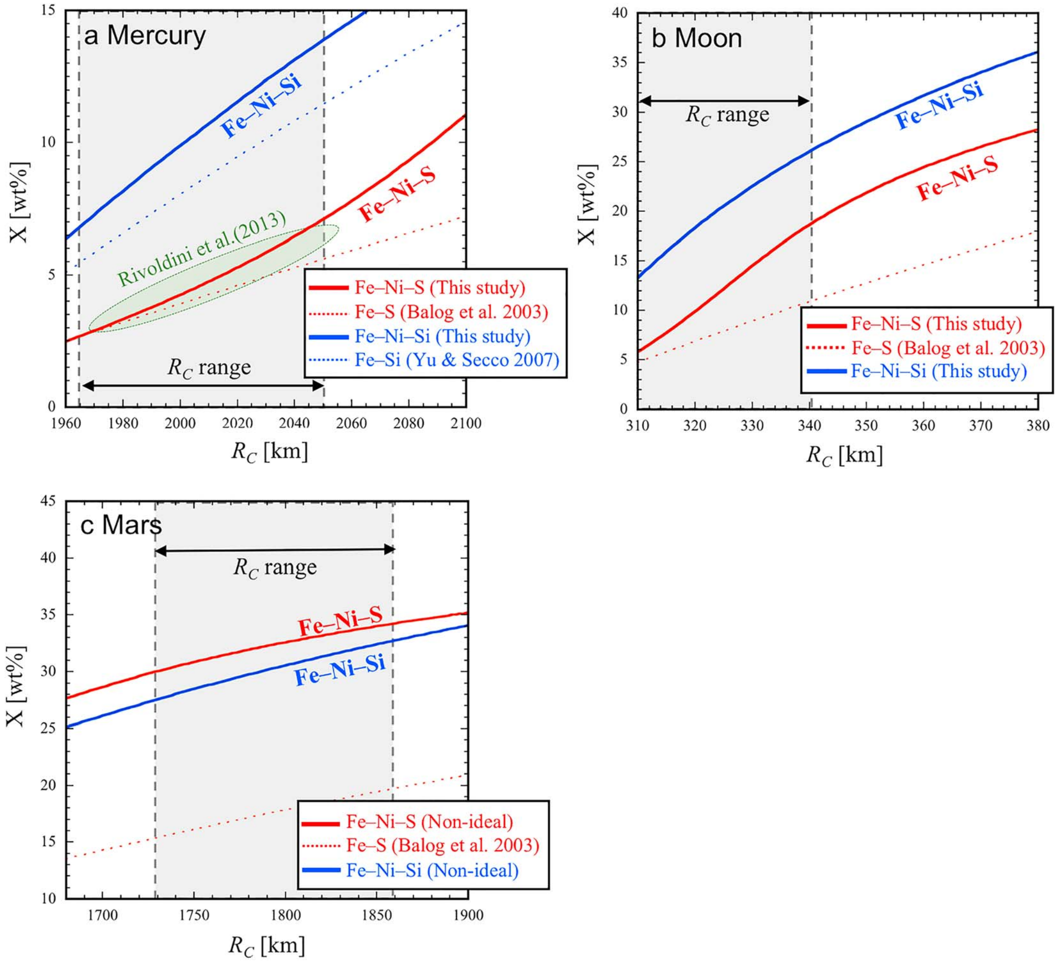


**Figure 6.** Relations between core radius ($R_C$) and S or Si content ($X$) in the core. The results of Fe-Ni-S and Fe-Ni-Si core models are respectively shown in red and blue curves (solid thick curve: elastic data of this study with nonideal mixing model, dotted curve: previous elastic data of Fe-10wt% S (Balog et al., 2003) or that of Fe-17wt% Si (Yu & Secco, 2008) with ideal mixing model). Possible $R_C$ range from MOI and geodesy data are indicated by gray hutch. (a) Mercury's core. Possible $R_C$ range indicated by gray hutch corresponds to 1,965–2,050 km (Mazarico et al., 2014). The green-hatched area indicates the 68% confidence interval for the reported liquid Fe-S core model (Rivoldini & Van Hoolst, 2013). (b) Lunar core. Possible $R_C$ range is 320 ± 20 km (Weber et al., 2011). (c) Martian core. Possible $R_C$ range from the MOI and tidal Love number corresponds to 1,729–1,859 km (Rivoldini et al., 2011).

properties (such as density, bulk modulus, and thermal expansivity) of these alloys, we used the nonideal mixing model for both the Fe-Ni-S and Fe-Ni-Si systems. All models fit the planet mass ($M$) exactly, and the LE concentration is calculated from the radius and average density of the core. The range of considered core radii is chosen such that it includes the measured mean moment of inertia ($MOI$). For all models, we assume a silicate shell structure and a liquid core with an adiabatic temperature profile. Details of the interior models of each body are given in Appendix C.

### 5.1. Mercury's Core

The calculated LE (S or Si) content in the Mercury core is shown as a function of a core radius ($R_C$) in Figure 6a. The range of core radii plotted in Figure 6a is in accord with measured MOI data (Mazarico et al., 2014; Table C2 ). To constrain the LE content more precisely, we take a value range for the $R_C$ of 1,965–2,050 km, as estimated from gravity field and spin state data (Hauck et al., 2013; Rivoldini & Van Hoolst, 2013). Our best estimates for the LE content in the core are S = 4.6 + 2.5/−2.0 wt% or Si = 10.5 +3.3/−3.7 wt%. The present estimate of S content is comparable with previously reported S content (4.5 ± 1.8 wt%; Rivoldini & Van Hoolst, 2013). Based on the estimated core compositions, the profiles of $V_P$ and $\rho$ in the

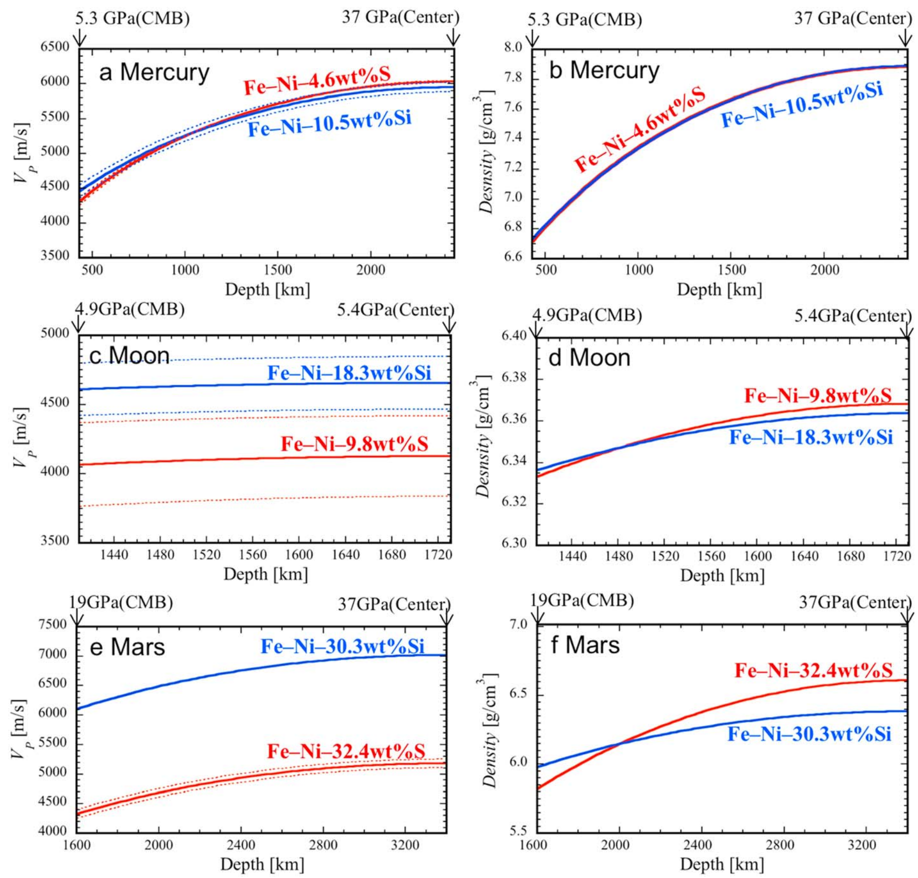


**Figure 7.** $V_P$ and density profiles of the planetary cores. Red and blue curves respectively represent profiles of Fe-Ni-S and Fe-Ni-Si core. Dotted curves indicate errors of the $V_P$ profile derived from the error of estimated S or Si content. (a,b) Mercury, (c,d) the Moon, and (e,f) Mars.

Mercury molten core are shown in Figures 7a and 7b. The differences in $V_P$ and density between Fe-Ni-4.6wt% S and Fe-Ni-10.5wt% Si are found to be small ($\Delta V_P$ ~ 150 m/s, $\Delta\rho$ ~ 0.01 g/cm$^3$) over the entire core range. Even if we take into account the error of LE content, the difference in $V_P$ and $\rho$ between S-rich and Si-rich cores are still small ($\Delta V_P$ ~ 290 m/s, $\Delta\rho$ ~ 0.03 g/cm$^3$).

### 5.2. Lunar Core

The relationship between estimated LE content and core radius ($R_C$) is shown in Figure 6b. If the $R_C$ of 320 ± 20 km (Weber et al., 2011), deduced from Apollo seismic data, is adopted, the estimated LE concentration in the core is S = 9.8 + 8.8/−7.9 wt% or Si = 18.3 + 7.7/−10.4 wt%. The seismic and density profiles of the lunar core are shown in Figures 7c and 7d. The $V_P$ of an Fe-Ni-S core ranges from 4,070 to 4,130 m/s. The $V_P$ of an Fe-Ni-Si core ranges from 4,610 to 4,660 m/s, which is clearly larger than in a S-rich core. However, the $V_P$ profile of the lunar core has a large uncertainty due to relatively large errors of estimated LE content which derives from $R_C$ error. If the $R_C$ is strictly constrained by geophysical measurements, the $V_P$ profile and thus LE chemistry in the lunar core could be determined. If the outer core $V_P$ of 4,100 ± 200 m/s reported by Weber et al. (2011) is adopted, this is consistent with the $V_P$ of Fe-Ni-S core of this study (4,070–4,130 m/s) whereas the $V_P$ of Fe-Ni-Si core (4,610–4,660 m/s) is significantly larger.

### 5.3. Martian Core

The LE content associated with core radii of Mars are shown in Figure 6c. For $R_C$ = 1,794 ± 65 km, which is estimated from the *MOI* and tidal Love number (Rivoldini et al., 2011), we find that the core contains either 32.4 + 1.8/−2.4 wt% of S or 30.3 + 2.4/−2.8 wt% of Si. This estimation of S concentration is larger than the previous estimates ranging from 14 to 36 wt% (14.2 wt%: Bertka & Fei, 1998;

16.2–17.4 wt%: Sanloup et al., 1999; 20–36 wt%: Zharkov & Gudkova, 2005; 22–25 wt%: Khan & Connolly, 2008; 16 + 1/−2 wt%: Rivoldini et al., 2011). Difference in estimated S amount in the Martian cores between this study and these previous studies results from significant difference between the elastic properties (in particular, density) of Fe-Ni-S of this study and those used in previous studies. The previous estimates of S content used the elastic properties of solid Fe and FeS (Bertka & Fei, 1998; Khan & Connolly, 2008; Sanloup et al., 1999; Zharkov & Gudkova, 2005), or liquid Fe and Fe-10wt%S (Rivoldini et al., 2011). The newly obtained elastic properties of liquid Fe-Ni-S in this study give an important update to the estimation of S content in Martian core. In addition, the present is also larger from chemical composition deduced from Martian meteorite ($X_S$ =14.2 wt%, Dreibus & Wänke, 1985; $X_S$ = 21.4 wt%, Taylor, 2013). If such large fractions of S in the core are discrepant from a geochemical perspective, then S may not be the sole LE in the Martian core.

Note that the liquidus phase of the Martian core, at the compositions found in this study, is either $(Fe,Ni)_{3-x}S_2$ (Fei et al., 2000; Stewart et al., 2007; Urakawa et al., 2018) or (Fe,Ni)Si (Kuwayama & Hirose, 2004) because the S or Si content in the core is richer than the eutectic composition (S = 16 wt% or Si = 25 wt%) at the Martian CMB. These phases will crystallize first and comprise the solid core when the temperature drops below the liquidus. This crystallization scheme will affect dynamo action in the Martian core.

The $V_P$ and $\rho$ profiles of the Martian core are shown in Figures 7e and 7f. The $V_P$ of an Fe-Ni-S core (4,320–5,180 m/s) is much smaller than that of an Fe-Ni-Si core (6,100–7,020 m/s), and the difference is large enough to be detected ($\Delta V_P$ ~ 1,780–1,840 m/s) even if we consider the error in $V_P$ profile. NASA's InSight mission will soon explore the interior structure of Mars through seismic sounding (Banerdt et al., 2013). The seismometers installed on the surface could observe core-interacting body wave phases if the magnitude of seismic events is large enough (Panning et al., 2016). Therefore, by comparing forthcoming seismic data with the present $V_P$ and density profiles, the plausible Martian core composition could be constrained.

## 6. Conclusions

The effect of pressure, temperature, and composition on sound velocity and density of liquid Fe-Ni-S and Fe-Ni-Si have been measured up to 14 GPa. The pressure dependence of sound velocity is well fitted by using the Birch-Murnaghan or Vinet equation of state. Obtained bulk modulus reduces with increasing S content, whereas it stays constant with variation of Si content. Based on measured elastic properties with the nonideal mixing model, we estimated the S or Si content in the cores of Mercury (4.6 wt% S or 10.5 wt% Si), the Moon (9.8 wt% S or 18.3 wt% Si), and Mars (32.4 wt% S or 30.3 wt% Si). In the core compositions of Mars and probably Moon, difference in sound velocity between the Fe-Ni-S and Fe-Ni-Si core is large enough to be detected.

In the case that a solid (inner) core exists and the outer core radius is assumed to be constant, LE content in the liquid core is considered as follows. If the core contains less LE than the eutectic composition in total, the LE content in the liquid core is more than that in total molten core because that LE generally partitions into the liquid phase. Hence, the estimated LE content in total molten core corresponds to a lower limit of LE content in the liquid core. In contrast, if the core contains LE more than eutectic composition, LE content in the liquid core would be less than that in total molten core. Thus, the LE content in this study shows upper limit. Mercury and Moon cores correspond to the former case. However, Mars requires much more LE in the core, suggesting that Mars corresponds to the latter case.

The LE contents in planetary cores tend to increase with heliocentric distance, that is, distance from the Sun. This trend highlights the important aspect that the outer terrestrial planet has formed in an environment richer in S or Si, suggesting that chemical zoning or variation in redox state may exist in the early inner solar system.

## Appendix A: X-ray CT Measurement

The X-ray radiography image was obtained with a pixel size of 1.43–1.51 μm. The CT measurement was carried out by rotating the press in 0.25–0.50° steps. The exposure time for each image was 150 ms. This setup enables a fast CT measurement (within ~3 min), which is advantageous for molten samples at high temperatures. The volumes of the samples were obtained from vertical stacking of the sample areas in the horizontal plane. The sample areas were measured, in horizontal cross section image (CT slice), by thresholding the clear contrast between the sample and surrounding BN using image processing software (Image J). The density of the sample was calculated from the sample volume and its weight. The density error estimate is mainly derived from uncertainty in selection of the image processing threshold. Details of density measurement using X-ray CT method are described elsewhere (Kuwabara et al., 2016). As shown in Figure 1a, high temperatures were generated using a cylindrical graphite furnace. Experimental temperatures were estimated from the electric power-temperature relationship at each load condition, which was calibrated in separate experiments with a thermocouple.

## Appendix B: Equations of State and Parameter Fitting

### B1. Murnaghan EoS

The effect of $P$ on the $V_P$ of liquid Fe-alloys has been expressed with the Murnaghan EoS (Jing et al., 2014). If the bulk modulus, $K$, is approximated by a linear function of pressure, $\rho$ and $K$ are described as follows (Murnaghan, 1937):

$$P = \frac{K_0}{K_0'}\left[\left(\frac{\rho}{\rho_0}\right)^{K'_0} - 1\right] \tag{B1}$$

$$K = K_0 + K'_0 P \tag{B2}$$

where $\rho_0$, $K_0$, and $K'_0$ indicate density, bulk modulus at ambient pressure, and its pressure derivative, respectively.

### B2. Birch-Murnaghan EoS

Based on the 3BM EoS, which is widely used for compression behavior of solid materials, $P$ and bulk modulus ($K$) are described as follows (Birch, 1952):

$$P = \frac{3}{2}K_0\left[\left(\frac{\rho}{\rho_0}\right)^{7/3} - \left(\frac{\rho}{\rho_0}\right)^{5/3}\right]\left\{1 + \frac{3}{4}(K'_0 - 4)\left[\left(\frac{\rho}{\rho_0}\right)^{2/3} - 1\right]\right\}, \tag{B3}$$

$$K = K_0\left(\frac{\rho}{\rho_0}\right)^{5/3}\left[1 + \frac{1}{2}(3K'_0 - 5)\left\{\left(\frac{\rho}{\rho_0}\right)^{2/3} - 1\right\} + \frac{27}{8}(K'_0 - 4)\left\{\left(\frac{\rho}{\rho_0}\right)^{2/3} - 1\right\}^2\right] \tag{B4}$$

where $K'_0$ is the derivative of the bulk modulus with respect to pressure, and the subscript 0 indicates values at ambient pressure.

### B3. Vinet EoS

The Vinet equation is written as (Vinet et al., 1989):

$$P = 3K_0\left(\frac{\rho}{\rho_0}\right)^{2/3}\left[1 - \left(\frac{\rho}{\rho_0}\right)^{-1/3}\right]\exp\left\{\frac{3}{2}(K'_0 - 1)\left[1 - \left(\frac{\rho}{\rho_0}\right)^{-1/3}\right]\right\}, \tag{B5}$$

$$K = \frac{3}{2}K_0\left(\frac{\rho}{\rho_0}\right)^{2/3}\left[\frac{4}{3} + \left(K'_0 - \frac{5}{3}\right)\left(\frac{\rho}{\rho_0}\right)^{-1/3} + (1 - K'_0)\left(\frac{\rho}{\rho_0}\right)^{-2/3}\right]\exp\left\{\frac{3}{2}(1 - K'_0)\left[\left(\frac{\rho}{\rho_0}\right)^{-1/3} - 1\right]\right\}, \tag{B6}$$

The thermal effect on $\rho$ is expressed as

$$\rho_T = \rho_{T0}\exp[-\alpha(T - T_0)], \tag{B7}$$

where $\rho_T$ is $\rho$ at temperature $T$, and $T_0$ is reference temperature. The temperature-corrected bulk modulus is calculated as

**Table C1**
*Mercury Mantle Profile*

| $R$ (km) | $P$ (GPa) | $T$ (K) | $\rho$ (kg/m$^3$) |
|---|---|---|---|
| 2,431 | 0.1 | 482 | 2,900 |
| 2,423 | 0.2 | 524 | 2,900 |
| 2,414 | 0.3 | 566 | 2,900 |
| 2,405 | 0.4 | 608 | 2,900 |
| 2,397 | 0.5 | 650 | 3,201 |
| 2,388 | 0.6 | 692 | 3,200 |
| 2,380 | 0.7 | 734 | 3,198 |
| 2,371 | 0.8 | 776 | 3,197 |
| 2,362 | 0.9 | 818 | 3,196 |
| 2,354 | 1.0 | 860 | 3,195 |
| 2,345 | 1.1 | 903 | 3,194 |
| 2,336 | 1.2 | 945 | 3,192 |
| 2,328 | 1.3 | 987 | 3,191 |
| 2,319 | 1.4 | 1029 | 3,190 |
| 2,310 | 1.5 | 1071 | 3,189 |
| 2,302 | 1.6 | 1113 | 3,187 |
| 2,293 | 1.7 | 1155 | 3,186 |
| 2,284 | 1.8 | 1197 | 3,185 |
| 2,276 | 1.9 | 1239 | 3,183 |
| 2,267 | 2.0 | 1281 | 3,182 |
| 2,259 | 2.1 | 1323 | 3,181 |
| 2,250 | 2.2 | 1365 | 3,179 |
| 2,241 | 2.3 | 1407 | 3,178 |
| 2,233 | 2.4 | 1449 | 3,176 |
| 2,224 | 2.6 | 1491 | 3,175 |
| 2,215 | 2.7 | 1533 | 3,174 |
| 2,207 | 2.8 | 1575 | 3,172 |
| 2,198 | 2.9 | 1617 | 3,171 |
| 2,189 | 3.0 | 1659 | 3,169 |
| 2,181 | 3.1 | 1701 | 3,168 |
| 2,172 | 3.2 | 1743 | 3,166 |
| 2,164 | 3.3 | 1786 | 3,165 |
| 2,155 | 3.4 | 1828 | 3,163 |
| 2,146 | 3.5 | 1870 | 3,162 |
| 2,138 | 3.6 | 1900 | 3,162 |
| 2,129 | 3.7 | 1900 | 3,165 |
| 2,120 | 3.8 | 1900 | 3,169 |
| 2,112 | 3.9 | 1900 | 3,172 |
| 2,103 | 4.0 | 1900 | 3,175 |
| 2,094 | 4.1 | 1900 | 3,179 |
| 2,086 | 4.3 | 1900 | 3,182 |
| 2,077 | 4.4 | 1900 | 3,186 |
| 2,068 | 4.5 | 1900 | 3,189 |
| 2,060 | 4.6 | 1900 | 3,192 |
| 2,051 | 4.7 | 1900 | 3,196 |
| 2,043 | 4.8 | 1900 | 3,199 |
| 2,034 | 4.9 | 1900 | 3,202 |
| 2,025 | 5.0 | 1900 | 3,206 |
| 2,017 | 5.1 | 1900 | 3,209 |
| 2,008 | 5.3 | 1900 | 3,212 |

$$K(\mathrm{P}_0, T) = K_0\left(\frac{\rho_T}{\rho_{T0}}\right)^{\delta}, \tag{B8}$$

where $\delta$ represents the Anderson-Grüneisen parameter, $\delta = -(1/\alpha K)(\mathrm{d}K/\mathrm{d}T)_P$ (Anderson, 1967).

For the isothermal settings, $V_P$ and/or $\rho$ data at each $P$-$T$ condition are fitted using a combination of equations of state ((B1), (B3), and (B5)) and finite strain equations ((B2), (B4), and (B6)) taking into account the thermal effect on density (equation (B7)) using the Anderson-Grüneisen relation ($\delta_T$ =

**Table C2**
*Models of Mercury Core*

| $R_C$ (km) | S content (wt%) | MOI |
|---|---|---|
| *Fe-Ni-S Core Model* | | |
| 1,960 | 2.5 | 0.337094 |
| 1,970 | 2.9 | 0.338128 |
| 1,980 | 3.3 | 0.339163 |
| 1,990 | 3.8 | 0.340200 |
| 2,000 | 4.2 | 0.341238 |
| 2,010 | 4.7 | 0.342275 |
| 2,020 | 5.3 | 0.343312 |
| 2,030 | 5.8 | 0.344347 |
| 2,040 | 6.4 | 0.345379 |
| 2,050 | 7.1 | 0.346406 |
| 2,060 | 7.8 | 0.347426 |
| 2,070 | 8.5 | 0.348437 |
| 2,080 | 9.3 | 0.349437 |
| 2,090 | 10.2 | 0.350424 |
| 2,100 | 11.1 | 0.351394 |
| *Fe-Ni-Si Core Model* | | |
| 1,960 | 6.4 | 0.337068 |
| 1,970 | 7.3 | 0.338107 |
| 1,980 | 8.2 | 0.339151 |
| 1,990 | 9.0 | 0.340200 |
| 2,000 | 9.9 | 0.341255 |
| 2,010 | 10.7 | 0.342316 |
| 2,020 | 11.5 | 0.343383 |
| 2,030 | 12.3 | 0.344455 |
| 2,040 | 13.1 | 0.345533 |
| 2,050 | 13.9 | 0.346616 |
| 2,060 | 14.6 | 0.347706 |
| 2,070 | 15.3 | 0.348801 |
| 2,080 | 16.0 | 0.349902 |
| 2,090 | 16.7 | 0.351009 |
| 2,100 | 17.3 | 0.352122 |

*Note.* MOI = moment of inertia.

$-(1/\alpha K_T)(\mathrm{d}K_T/\mathrm{d}T)_P)$. For the fit to $V_P$, equation (2) and the relation $K_S = (1{+}\alpha\gamma T)K_T$ was used. As a result of the fitting, $K_{T0}$ and $K'_T$ are obtained together with $\alpha_0$ and $\delta_T$ as listed in Table 4. Since temperature conditions of the data are taken into account in the fitting procedure, no prior temperature correction is applied to the data.

For the isentropic setting, no temperature correction is applied to the data prior to the fitting. To describe $V_P$ and $\rho$ at ($P$, $T$) using the elastic parameters, we consider following a $P$-$T$ path starting from reference conditions ($P_0$, $T_0$). In the $P$-$T$ path for isentropic setting, we start with an isobaric heating at $P_0$ from $T_0$ to $T_1$ (a foot of isentrope), followed by an isentropic compression from ($P_0$, $T_1$) to ($P$, $T$) with an isentropic EoS for the compression along isentrope. Details of the isentropic setting are described in Verhoeven et al. (2005). All the elastic parameters ($K_{S0}$, $K'_S$, $\rho_0$, $\alpha_0$, $\delta_S$, and $\gamma$) that follow the $P$-$T$ path described above are estimated simultaneously by fitting the equations describing the isentropic setting to the $V_P$ and $\rho$ data (see Appendix A of Verhoeven et al. (2005) for details). In this study, the elastic parameters ($K_{S0}$, $K'_S$, $\rho_0$, $\alpha_0$, and $\delta_S$) are obtained from the isentropic fitting as listed in Table 3 assuming fixed $\gamma$.

Isothermal and isentropic elastic properties were obtained independently from each fit. To check the consistency between isothermal and isentropic elastic properties, we calculated isentropic $K_{S0}$ and $K'_S$ from obtained $K_{T0}$ and $K'_T$ based on the conversion relation of $K_{S0} = (1{+}\alpha_0\gamma T)K_{T0}$ using $\alpha_0$, $\gamma$, and $T$ listed in Table 4. The $K_{S0}$ and $K'_S$ obtained from isentropic fit are quite consistent with those calculated from the conversion of isothermal properties, suggesting that elastic properties obtained from isentropic fit and from isothermal fit in this study are consistent each other.

**Table C3**
*Models of Lunar Core*

| $R_C$ (km) | S content (wt%) | MOI |
|---|---|---|
| *Fe-Ni-S Core Model* | | |
| 310 | 5.8 | 0.3931131 |
| 315 | 7.7 | 0.3931153 |
| 320 | 9.8 | 0.3931176 |
| 325 | 12.2 | 0.3931200 |
| 330 | 14.5 | 0.3931223 |
| 335 | 16.7 | 0.3931248 |
| 340 | 18.7 | 0.3931272 |
| 345 | 20.4 | 0.3931297 |
| 350 | 21.9 | 0.3931322 |
| 355 | 23.2 | 0.3931347 |
| 360 | 24.5 | 0.3931373 |
| 365 | 25.5 | 0.3931400 |
| 370 | 26.5 | 0.3931426 |
| 375 | 27.4 | 0.3931453 |
| 380 | 28.3 | 0.3931480 |
| *Fe-Ni-Si Core Model* | | |
| 310 | 13.3 | 0.3931131 |
| 315 | 15.9 | 0.3931154 |
| 320 | 18.3 | 0.3931177 |
| 325 | 20.5 | 0.3931200 |
| 330 | 22.5 | 0.3931224 |
| 335 | 24.4 | 0.3931248 |
| 340 | 26.0 | 0.3931273 |
| 345 | 27.6 | 0.3931298 |
| 350 | 29.1 | 0.3931323 |
| 355 | 30.4 | 0.3931349 |
| 360 | 31.7 | 0.3931375 |
| 365 | 32.9 | 0.3931401 |
| 370 | 34.0 | 0.3931428 |
| 375 | 35.1 | 0.3931455 |
| 380 | 36.1 | 0.3931483 |

*Note.* MOI = moment of inertia.

# Appendix C: Interior Models of Planets

## C1. Mercury

Mercury has been considered to have a relatively large core compared with other terrestrial planets. Although sulfur has usually been assumed to be the core LE, a significant amount of silicon could be present in Mercury's core because of the highly reducing formation conditions of Mercury (Nittler et al., 2011). The modeling related to the interior structure of Mercury follows that of previous studies (Dumberry & Rivoldini,

**Table C4**
*Major Element Composition Models of Martian Mantle*

| Element | DW(85)[a] | MM(03)[b] |
|---|---|---|
| CaO | 2.4 | 1.9 |
| FeO | 17.9 | 16.9 |
| MgO | 30.2 | 29.1 |
| $Al_2O_3$ | 3.0 | 2.5 |
| $SiO_2$ | 44.4 | 47.1 |
| $Na_2O$ | 0.5 | 1.2 |

*Note.* Numbers correspond to wt%.
[a]Dreibus and Wanke (1985). [b]Mohapatra and Murty (2003).

**Table C5**
*Mars Mantle Profile*

| *R* (km) | *P* (GPa) | *T* (K) | $\rho$ (kg/m$^3$) |
|---|---|---|---|
| 3,358 | 0.3 | 446 | 2,700 |
| 3,326 | 0.6 | 620 | 2,700 |
| 3,294 | 1.0 | 788 | 3,486 |
| 3,262 | 1.4 | 930 | 3,482 |
| 3,230 | 1.8 | 1062 | 3,479 |
| 3,198 | 2.2 | 1184 | 3,476 |
| 3,166 | 2.6 | 1298 | 3,475 |
| 3,134 | 3.0 | 1401 | 3,475 |
| 3,102 | 3.4 | 1496 | 3,476 |
| 3,070 | 3.8 | 1581 | 3,478 |
| 3,038 | 4.2 | 1656 | 3,482 |
| 3,007 | 4.6 | 1722 | 3,486 |
| 2,975 | 5.0 | 1779 | 3,492 |
| 2,943 | 5.4 | 1818 | 3,499 |
| 2,911 | 5.8 | 1827 | 3,511 |
| 2,879 | 6.2 | 1835 | 3,522 |
| 2,847 | 6.6 | 1844 | 3,532 |
| 2,815 | 7.0 | 1853 | 3,543 |
| 2,783 | 7.4 | 1862 | 3,554 |
| 2,751 | 7.7 | 1871 | 3,564 |
| 2,719 | 8.1 | 1879 | 3,574 |
| 2,687 | 8.5 | 1888 | 3,585 |
| 2,656 | 8.9 | 1897 | 3,595 |
| 2,624 | 9.3 | 1906 | 3,605 |
| 2,592 | 9.7 | 1914 | 3,615 |
| 2,560 | 10.1 | 1923 | 3,626 |
| 2,528 | 10.4 | 1932 | 3,636 |
| 2,496 | 10.8 | 1941 | 3,647 |
| 2,464 | 11.2 | 1950 | 3,659 |
| 2,432 | 11.6 | 1958 | 3,672 |
| 2,400 | 12.0 | 1967 | 3,689 |
| 2,368 | 12.3 | 1976 | 3,702 |
| 2,336 | 12.7 | 1985 | 3,719 |
| 2,305 | 13.1 | 1994 | 3,743 |
| 2,273 | 13.5 | 2002 | 3,828 |
| 2,241 | 13.9 | 2011 | 3,866 |
| 2,209 | 14.3 | 2020 | 3,878 |
| 2,177 | 14.7 | 2029 | 3,889 |
| 2,145 | 15.1 | 2038 | 3,900 |
| 2,113 | 15.5 | 2046 | 3,911 |
| 2,081 | 15.8 | 2055 | 3,923 |
| 2,049 | 16.2 | 2064 | 3,938 |
| 2,017 | 16.6 | 2073 | 3,956 |
| 1,985 | 17.0 | 2081 | 3,976 |
| 1,954 | 17.4 | 2090 | 3,992 |
| 1,922 | 17.8 | 2099 | 4,004 |
| 1,890 | 18.2 | 2108 | 4,019 |
| 1,858 | 18.6 | 2117 | 4,038 |
| 1,826 | 19.0 | 2125 | 4,046 |
| 1,794 | 19.4 | 2134 | 4,053 |

2015; Rivoldini & Van Hoolst, 2013). We assumed a thickness of 35 km (Padovan et al., 2015) and an average density of 2,900 kg/cm$^3$ for the crust, and a mixture of olivine (60 wt%) and ortho-pyroxene (40 wt%) for the mantle. The temperature in the mantle is conductive and anchored at the CMB (1900 K) and at the surface (440 K). The density profile of Mercury crust and mantle is listed in Table C1. The calculated results for the Mercury core model are listed in Table C2.

**Table C6**
*Models of Martian Core*

| $R_C$ (km) | S content (wt%) | MOI |
|---|---|---|
| *Fe-Ni-S Core Model* | | |
| 1,700 | 28.6 | 0.363143 |
| 1,710 | 29.1 | 0.363225 |
| 1,720 | 29.6 | 0.363308 |
| 1,730 | 30.0 | 0.363392 |
| 1,740 | 30.5 | 0.363476 |
| 1,750 | 30.9 | 0.363560 |
| 1,760 | 31.2 | 0.363645 |
| 1,770 | 31.6 | 0.363730 |
| 1,780 | 31.9 | 0.363816 |
| 1,790 | 32.3 | 0.363902 |
| 1,800 | 32.6 | 0.363988 |
| 1,810 | 32.9 | 0.364075 |
| 1,820 | 33.2 | 0.364162 |
| 1,830 | 33.5 | 0.364250 |
| 1,840 | 33.7 | 0.364338 |
| 1,850 | 34.0 | 0.364426 |
| 1,860 | 34.3 | 0.364515 |
| 1,870 | 34.5 | 0.364604 |
| 1,880 | 34.7 | 0.364693 |
| 1,890 | 35.0 | 0.364784 |
| 1,900 | 35.2 | 0.364874 |
| *Fe-Ni-Si Core Model* | | |
| 1,700 | 26.1 | 0.363260 |
| 1,710 | 26.6 | 0.363349 |
| 1,720 | 27.1 | 0.363439 |
| 1,730 | 27.6 | 0.363530 |
| 1,740 | 28.0 | 0.363621 |
| 1,750 | 28.5 | 0.363713 |
| 1,760 | 28.9 | 0.363805 |
| 1,770 | 29.3 | 0.363898 |
| 1,780 | 29.7 | 0.363991 |
| 1,790 | 30.2 | 0.364085 |
| 1,800 | 30.6 | 0.364180 |
| 1,810 | 30.9 | 0.364274 |
| 1,820 | 31.3 | 0.364370 |
| 1,830 | 31.7 | 0.364466 |
| 1,840 | 32.1 | 0.364563 |
| 1,850 | 32.4 | 0.364660 |
| 1,860 | 32.8 | 0.364758 |
| 1,870 | 33.1 | 0.364856 |
| 1,880 | 33.4 | 0.364955 |
| 1,890 | 33.8 | 0.365055 |
| 1,900 | 34.1 | 0.365156 |

*Note*. MOI = moment of inertia.

## C2. Moon

Interior structural models of the Moon have been updated recently from high-resolution lunar gravity data (Williams et al., 2014), Apollo seismic data (Garcia et al., 2011; Weber et al., 2011), and a combination thereof (Matsumoto et al., 2015). Taken together, these studies proposed that the Moon's core radius ranges from 200 to 420 km, and with LE, assuming sulfur, below 25 wt%. Here, we model the interior structure of the Moon using the silicate shell structures inferred by Weber et al. (2011), which has been deduced from Apollo seismological data. To have fully liquid cores in our models, the temperature at the CMB was set to 1800 K. The calculated results of the lunar core model are listed in Table C3.

## C3. Mars

Because seismic measurements for Mars are not yet available, constraints on interior structure models of Mars are usually obtained from geodesy data and assumptions of the planet's thermal state and composition (Sohl & Spohn, 1997; Zharkov & Gudkova, 2000; Urakawa et al., 2004; Khan & Connolly, 2008; Rivoldini et al., 2011). Bulk composition models of Mars deduced from Martian meteorites show that sulfur is likely the most abundant LE in its core (Dreibus & Wänke, 1985). Other LEs that could be present, together with sulfur, in smaller amounts are hydrogen (Zharkov & Gudkova, 2000) and silicon (Mohapatra & Murty, 2003).

Here, we consider two model settings for the Martian core and mantle composition: (i) an Fe-Ni-S core with the mantle composition suggested by Dreibus and Wänke (1985) and (ii) an Fe-Ni-Si core with the mantle composition suggested by Mohapatra and Murty (2003). The mantle compositions according to these models are listed in Table C4. Mantle mineralogies for the two compositions have been computed with the Perple_X program (Connolly, 2009) using thermodynamic data derived by Stixrude and Lithgow-Bertelloni (2011). The crust thickness and average density were fixed to 55 km and 2,700 kg/cm$^3$ (Wieczorek & Zuber, 2004). We have adopted a temperature profile of the mantle deduced from a recent study about the thermal evolution of Mars (Case 21 in Plesa et al., 2016) and set the temperature at the CMB to 2105–2160 K, depending on the $R_C$. For these models, we provide a range of core radii and compositions that agree with the most recent mass and MOI estimates of Mars (Konopliv et al., 2016). The density profile of Martian crust and mantle is listed in Table C5. The calculated results of the Martian core models are listed in Table C6.

**Acknowledgments**

The authors acknowledge S. Kamada, S. Kuwabara, R. Saito, Y. Kono, H. Tobe, Y. Tange, Y. Katayama, H. Kaneko, Y. Suzuki, S. Yamamoto, and Y. Takahashi for their technical support and discussions. The authors are grateful to two anonymous reviewers for their constructive comments. This work is partly supported by Grants-in-Aid for scientific research from the Ministry of Education, Culture, Sport, and Science and Technology (MEXT) of the Japanese Government to H. T. (23340159, 26247089, and 15H05828), K. N. (26800231), and S. U. (23340129). This work was also partly supported by the Belgian PRODEX program managed by the European Space Agency in collaboration with the Belgian Federal Science Policy Office and by the Belgian Federal Science Policy Office (BR/143/A2/COME-IN). The synchrotron radiation experiments have been performed under contract of the SPring-8 facility (proposals: 2013B1488, 2014A1161, 2014A3787, 2014B1319, 2015A1330, 2015A3787, 2015B1555, 2015B3790, 2016A3787, 2016B1518, and 2016B3781). A part of this work was performed under the Shared Use Program of JAEA and QST Facilities (proposals: 2014A-E24, 2015A-E20, 2015B-E20, 2016A-E22, and 2016B-H07) supported by JAEA, QST Advanced Characterization Nanotechnology Platform as a program of "Nanotechnology Platform" of MEXT (proposals: A-15-AE-0040, A-16-QS-0014, and A-16-QS-0021). The data for this paper are listed in Tables 1 and C1 and also available by contacting the corresponding author H. T. at terasaki@ess.sci.osaka-u.ac.jp.

## References

Alfè, D., Gillan, M. J., & Price, G. D. (2003). Thermodynamics from first principles: Temperature and composition of the Earth's core. *Mineralogical Magazine*, *67*(1), 113–123. https://doi.org/10.1180/0026461026610089

Anderson, O. L. (1967). Equation for thermal expansivity in planetary interiors. *Journal of Geophysical Research*, *72*(14), 3661–3668. https://doi.org/10.1029/JZ072i014p03661

Anderson, W. W., & Ahrens, T. J. (1994). An equation of state for liquid iron and implications for the Earth's core. *Journal of Geophysical Research*, *99*(B3), 4273–4284. https://doi.org/10.1029/93JB03158

Antonangeli, D., Morard, G., Schmerr, N. C., Komabayashi, T., Krisch, M., Fiquet, G., & Fei, Y. (2015). Toward a mineral physics reference model for the Moon's core. *Proceedings of the National Academy of Sciences of the United States of America*, *112*(13), 3916–3919. https://doi.org/10.1073/pnas.1417490112

Balog, P. S., Secco, R. A., Rubie, D. C., & Frost, D. J. (2003). Equation of state of liquid Fe-10 wt % S: Implications for the metallic cores of planetary bodies. *Journal of Geophysical Research*, *108*(B2), 2124. https://doi.org/10.1029/2001JB001646

Banerdt, W. B., Smrekar, S., Lognonné, P., Spohn, T., Asmar, S. W., Banfield, D., et al. (2013). INSIGHT: A discovery mission to explore the interior of Mars. *44th Lunar Planet Sci Conf* abstract, 1915

Bertka, C. M., & Fei, Y. (1998). Density profile of and SNC model Martian interior and the moment-of-inertia factor of Mars. *Earth and Planetary Science Letters*, *157*(1-2), 79–88. https://doi.org/10.1016/S0012-821X(98)00030-2

Birch, F. (1952). Elasticity and constitution of the Earth's interior. *Journal of Geophysical Research*, *57*(2), 227–286. https://doi.org/10.1029/JZ057i002p00227

Brearley, A. J., & Jones, R. H. (1998). Chondritic meteorites. In J. J. Papike (Ed.), *Planetary materials*, *Reviews in Mineralogy*, (Vol. 36, pp. 3-1–3-398). Washington DC: Mineralogical Society of America.

Buono, A. S., & Walker, D. (2011). The Fe-rich liquidus in the Fe-FeS system from 1 bar to 10 GPa. *Geochimica et Cosmochimica Acta*, *75*(8), 2072–2087. https://doi.org/10.1016/j.gca.2011.01.030

Cohen, R. E., Gulseren, O., & Hemley, R. J. (2000). Accuracy of equation-of-state formulations. *American Mineralogist*, *85*(2), 338–344. https://doi.org/10.2138/am-2000-2-312

Connolly, J. A. D. (2009). The geodynamic equation of state: What and how. *Geochemistry, Geophysics, Geosystems*, *10*, Q10014. https://doi.org/10.1029/2009gc002540

Dreibus, G., & Wänke, H. (1985). Mars, a volatile-rich planet. *Meteoritics*, *20*, 367–381.

Dumay, C., & Cramb, A. W. (1995). Density and interfacial tension of liquid Fe–Si alloys. *Metallurgical and Materials Transactions B*, *26B*, 173–176. https://doi.org/10.1007/bf02648989

Dumberry, M., & Rivoldini, A. (2015). Mercury's inner core size and core-crystallization regime. *Icarus*, *248*, 254–268. https://doi.org/10.1016/j.icarus.2014.10.038

Fei, Y., Li, J., Bertka, C. M., & Prewitt, C. T. (2000). Structure and bulk modulus of $Fe_3S$, a new iron-sulfur compound. *American Mineralogist*, *85*(11-12), 1830–1833. https://doi.org/10.2138/am-2000-11-1229

Garcia, R., Gagnepain-Beyneix, J., Chevrot, S., & Lognonné, P. (2011). Very preliminary reference Moon model. *Physics of the Earth and Planetary Interiors*, *188*(1-2), 96–113. https://doi.org/10.1016/j.pepi.2011.06.015

Hauck, S. A. II, Margot, J. L., Solomon, S. C., Phillips, R. J., Johnson, C. L., Lemoine, F. G., et al. (2013). The curious case of Mercury's internal structure. *Journal of Geophysical Research: Planets*, *118*, 1204–1220. https://doi.org/10.1002/jgre.20091

Higo, Y., Kono, Y., Inoue, T., Irifune, T., & Funakoshi, K. (2009). A system for measuring elastic wave velocity under high pressure and high temperature using a combination of ultrasonic measurement and the multi-anvil apparatus at SPring-8. *Journal of Synchrotron Radiation*, *16*(6), 762–768. https://doi.org/10.1107/S0909049509034980

Javoy, M., Kaminski, E., Guyot, F., Andrault, D., Sanloup, C., Moreira, M., et al. (2010). The chemical composition of the Earth: Enstatite chondrite models. *Earth and Planetary Science Letters*, *293*(3-4), 259–268. https://doi.org/10.1016/j.epsl.2010.02.033

Jing, Z., Wang, Y., Kono, Y., Yu, T., Sakamaki, T., Park, C., et al. (2014). Sound velocity of Fe–S liquids at high pressure: Implications for the Moon's molten outer core. *Earth and Planetary Science Letters*, *396*, 78–87. https://doi.org/10.1016/j.epsl.2014.04.015

Kaiura, G. H., & Toguri, J. M. (1979). Densities of the molten FeS, FeS-$CuS_2$ and Fe-S-O systems-Utilizing a bottom-balance Archimedean technique. *Canadian Metallurgical Quarterly*, *18*(2), 155–164. https://doi.org/10.1179/cmq.1979.18.2.155

Katayama, Y. (1996). Density measurements of non-crystalline materials under high pressure and high temperature. *High Pressure Research*, *14*(4-6), 383–391. https://doi.org/10.1080/08957959608201424

Kawaguchi, I. S., Nakajima, Y., Hirose, K., Komabayashi, T., Ozawa, H., Tateno, S., et al. (2017). Sound velocity of liquid Fe-Ni-S at high pressure. *Journal of Geophysical Research: Solid Earth*, *122*, 3624–3634. https://doi.org/10.1002/2016JB013609

Kawai, Y., Mori, K., Kishimoto, M., Ishikura, K., & Shimoda, S. (1974). Surface tension of liquid Fe-C-Si alloys (In Japanese text with English abstract). *Tetsu to Hagane*, *60*(1), 29–37. https://doi.org/10.2355/tetsutohagane1955.60.1_29

Khan, A., & Connolly, J. A. D. (2008). Constraining the composition and thermal state of Mars from inversion of geophysical data. *Journal of Geophysical Research*, *113*(E7), E07003. https://doi.org/10.1029/2007JE002996

Kono, Y., Park, C., Sakamaki, T., Kenny-Benson, C., Shen, G., & Wang, Y. (2012). Simultaneous structure and elastic wave velocity measurement of $SiO_2$ glass at high pressures and high temperatures in a Paris-Edinburgh cell. *The Review of Scientific Instruments*, *83*, 033905. https://doi.org/10.1063/1.3698000

Konopliv, A. S., Park, R. S., & Folkner, W. M. (2016). An improved JPL Mars gravity field and orientation from Mars orbiter and lander tracking data. *Icarus*, *274*, 253–260. https://doi.org/10.1016/j.icarus.2016.02.052

Kuwabara, S., Terasaki, H., Nishida, K., Shimoyama, Y., Takubo, Y., Higo, Y., et al. (2016). Sound velocity and elastic properties of Fe–Ni and Fe–Ni–C liquids at high pressure. *Physics and Chemistry of Minerals*, *43*(3), 229–236. https://doi.org/10.1007/s00269-015-0789-y

Kuwayama, Y., & Hirose, K. (2004). Phase relations in the system Fe-FeSi at 21 GPa. *American Mineralogist*, *89*(2-3), 273–276. https://doi.org/10.2138/am-2004-2-303

Malavergne, V., Toplis, M. J., Berthet, S., & Jones, J. (2010). Highly reducing conditions during core formation on Mercury: Implications for internal structure and the origin of a magnetic field. *Icarus*, *206*(1), 199–209. https://doi.org/10.1016/j.icarus.2009.09.001

Margot, J. L., Peale, S. J., Jurgens, R. F., Slade, M. A., & Holin, I. V. (2007). Large longitude libration of Mercury reveals a molten core. *Science*, *316*(5825), 710–714. https://doi.org/10.1126/science.1140514

Matsui, M. (2009). Temperature-pressure-volume equation of state of the B1 phase of sodium chloride. *Physics of the Earth and Planetary Interiors*, *174*(1-4), 93–97. https://doi.org/10.1016/j.pepi.2008.05.013

Matsumoto, K., Yamada, R., Kikuchi, F., Kamata, S., Ishihara, Y., Iwata, T., et al. (2015). Internal structure of the Moon inferred from Apollo seismic data and selenodetic data from GRAIL and LLR. *Geophysical Research Letters*, *42*, 7351–7358. https://doi.org/10.1002/2015GL065335

Mazarico, E., Genova, A., Goossens, S., Lemoine, F. G., Neumann, G. A., Zuber, M. T., et al. (2014). The gravity field, orientation, and ephemeris of Mercury from MESSENGER observations after three years in orbit. *Journal of Geophysical Research: Planets*, *119*, 2417–2436. https://doi.org/10.1002/2014JE004675

Mittlefehldt, D. W., McCoy, T. J., Goodrich, C. A., & Kracher, A. (1998). Non-chondritic meteorites from asteroidal bodies. In J. J. Papike (Ed.), *Planetary materials*, *Reviews in Mineralogy*, (Vol. 36, pp. 4-1–4-195). Washington DC: Mineralogical Society of America.

Mohapatra, R. K., & Murty, S. V. S. (2003). Precursors of Mars: Constraints from nitrogen and oxygen isotopic compositions of martian meteorites. *Meteoritics and Planetary Science*, *38*(2), 225–241. https://doi.org/10.1111/j.1945-5100.2003.tb00261.x

Morard, G., Garbarino, G., Antonangeli, D., Andrault, D., Guignot, N., Siebert, J., et al. (2013). Density measurements and structural properties of liquid and amorphous metals under high pressure. *High Pressure Research*, *34*(1), 9–21. https://doi.org/10.1080/08957959.2013.860137

Morard, G., Siebert, J., Andrault, D., Guignot, N., Garbarino, G., Guyot, F., & Antonangeli, D. (2013). The Earth's core composition from high pressure density measurements of liquid iron alloys. *Earth and Planetary Science Letters*, *373*, 169–178. https://doi.org/10.1016/j.epsl.2013.04.040

Murnaghan, F. D. (1937). Finite deformation of an elastic solid. *American Journal of Mathematics*, *59*(2), 235–260. https://doi.org/10.2307/2371405

Nagamori, M. (1969). Density of molten Ag-S, Cu-S, Fe-S, and Ni-S systems. *Transactions of the Metallurgical Society of the American Institute of Mechanical Engineers*, *245*, 1897–1902.

Nakajima, Y., Imada, S., Hirose, K., Komabayashi, T., Ozawa, H., Tateno, S., et al. (2015). Carbon-depleted outer core revealed by sound velocity measurements of liquid iron-carbon alloy. *Nature Communications*, *6*, 8942. https://doi.org/10.1038/ncomms9942

Nasch, P. M., Manghnani, M. H., & Secco, R. A. (1997). Anomalous behavior of sound velocity and attenuation in liquid Fe–Ni–S. *Science*, *277*(5323), 219–221. https://doi.org/10.1126/science.277.5323.219

Nishida, K., Kono, Y., Terasaki, H., Takahashi, S., Ishii, M., Shimoyama, Y., et al. (2013). Sound velocity measurements in liquid Fe–S at high pressure: Implications for Earth's and lunar cores. *Earth and Planetary Science Letters*, *362*, 182–186. https://doi.org/10.1016/j.epsl.2012.11.042

Nishida, K., Suzuki, A., Terasaki, H., Shibazaki, Y., Higo, Y., Kuwabara, S., et al. (2016). Towards a consensus on the pressure and composition dependence of sound velocity in the liquid Fe-S system. *Physics of the Earth and Planetary Interiors*, *257*, 230–239. https://doi.org/10.1016/j.pepi.2016.06.009

Nishida, K., Terasaki, H., Ohtani, E., & Suzuki, A. (2008). The effect of sulphur content on density of the liquid Fe-S at high pressure. *Physics and Chemistry of Minerals*, *35*(7), 417–423. https://doi.org/10.1007/s00269-008-0236-4

Nittler, L. R., Starr, R. D., Weider, S. Z., McCoy, T. J., Boynton, W. V., Ebel, D. S., et al. (2011). The major-element composition of Mercury's surface from MESSENGER X-ray spectrometry. *Science*, *333*(6051), 1847–1850. https://doi.org/10.1126/science.1211567

Padovan, S., Wieczorek, M. A., Margot, J.-L., Tosi, N., & Solomon, S. C. (2015). Thickness of the crust of Mercury from geoid-to-topography ratios. *Geophysical Research Letters*, *42*, 1029–1038. https://doi.org/10.1002/2014GL062487

Palme, H., & Jones, A. (2005). Solar system abundances of the elements. In A. M. Davis (Ed.) *Meteorites, comets, and planets*, Vol. 1, H. D. Holland, & K. K. Turekian (Eds.) *Treatise on Geochemistry*, Oxford, Elsevier-Pergamon, pp. 41–61.

Panning, M. P., Lognonné, P., Bruce Banerdt, W., Garcia, R., Golombek, M., Kedar, S., et al. (2016). Planned products of the Mars Structure Service for the InSight mission to Mars. *Space Science Reviews*, *211*(1-4), 611–650. https://doi.org/10.1007/s11214-016-0317-5

Plesa, A.-C., Grott, M., Tosi, N., Breuer, D., Spohn, T., & Wieczorek, M. A. (2016). How large are present-day heat flux variations across the surface of Mars? *Journal of Geophysical Research: Planets*, *121*, 2386–2403. https://doi.org/10.1002/2016JE005126

Rivoldini, A., & Van Hoolst, T. (2013). The interior structure of Mercury constrained by the low-degree gravity field and the rotation of Mercury. *Earth and Planetary Science Letters*, *377-378*, 62–72. https://doi.org/10.1016/j.epsl.2013.07.021

Rivoldini, A., Van Hoolst, T., Verhoeven, O., Mocquet, A., & Dehant, V. (2011). Geodesy constraints on the interior structure and composition of Mars. *Icarus*, *213*(2), 451–472. https://doi.org/10.1016/j.icarus.2011.03.024

Rubie, D. C., Jacobson, S. A., Morbidelli, A., O'Brien, D. P., Young, E. D., de Vries, J., et al. (2015). Accretion and differentiation of the terrestrial planets with implications for the compositions of early-formed Solar System bodies and accretion of water. *Icarus*, *248*, 89–108. https://doi.org/10.1016/j.icarus.2014.10.015

Sanloup, C., Fiquet, G., Gregoryanz, E., Morard, G., & Mezouar, M. (2004). Effect of Si on liquid Fe compressibility: Implications for sound velocity in core materials. *Geophysical Research Letters*, *31*, L07604. https://doi.org/10.1029/2004GL019526

Sanloup, C., Guyot, F., Gillet, P., & Fei, Y. (2002). Physical properties of liquid Fe alloys at high pressure and their bearings on the nature of metallic planetary cores. *Journal of Geophysical Research*, *107*(B11), ECV 4-1–ECV 4-9. https://doi.org/10.1029/2001JB000808

Sanloup, C., Guyot, F., Gillet, P., Fiquet, G., Mezouar, M., & Martinez, I. (2000). Density measurements of liquid Fe-S at high-pressure. *Geophysical Research Letters*, *27*(6), 811–814. https://doi.org/10.1029/1999GL008431

Sanloup, C., Jambon, A., & Gillet, P. (1999). A simple chondritic model of Mars. *Physics of the Earth and Planetary Interiors*, *112*(1-2), 43–54. https://doi.org/10.1016/S0031-9201(98)00175-7

Shimoyama, Y., Terasaki, H., Urakawa, S., Takubo, Y., Kuwabara, S., Kishimoto, S., et al. (2016). Thermoelastic properties of liquid Fe-C revealed by sound velocity and density measurements at high pressure. *Journal of Geophysical Research: Solid Earth*, *121*, 7984–7995. https://doi.org/10.1002/2016JB012968

Shobu, T., Tozawa, K., Shiwaku, H., Konishi, H., Inami, T., Harami, T., & Mizuki, J. (2007). Wide band energy beamline using Si(111) crystal monochrometers at BL22XU in SPring-8. *AIP Conference Proceedings*, *879*, 902. https://doi.org/10.1063/1.2436207

Smith, D. E., Zuber, M. T., Phillips, R. J., Solomon, S. C., Hauck, S. A., Lemoine, F. G., et al. (2012). Gravity field and internal structure of Mercury from MESSENGER. *Science*, *336*(6078), 214–217. https://doi.org/10.1126/science.1218809

Sohl, F., & Spohn, T. (1997). The interior structure of Mars: Implications from SNC meteorites. *Journal of Geophysical Research*, *102*(E1), 1613–1635. https://doi.org/10.1029/96JE03419

Steenstra, E. S., Rai, N., Knibbe, J. S., Lin, Y. H., & van Westrenen, W. (2016). New geochemical models of core formation in the Moon from metal–silicate partitioning of 15 siderophile elements. *Earth and Planetary Science Letters*, *441*, 1–9. https://doi.org/10.1016/j.epsl.2016.02.028

Stewart, A. J., Schmidt, M. W., van Westrenen, W., & Liebske, C. (2007). Mars: A new core-crystallization regime. *Science*, *316*(5829), 1323–1325. https://doi.org/10.1126/science.1140549

Stixrude, L., & Lithgow-Bertelloni, C. (2011). Thermodynamics of mantle minerals—II. Phase equilibria. *Geophysical Journal International*, *184*(3), 1180–1213. https://doi.org/10.1111/j.1365-246X.2010.04890.x

Suzuki, Y., Uesugi, K., Takimoto, N., Fukui, T., Aoyama, K., Takeuchi, A., et al.(2004). Construction and commissioning of A 248 m-long beamline with X-ray undulator light source. *AIP Conference Proceedings*, *705*, 344. https://doi.org/10.1063/1.1757804

Tange, Y., Nishihara, Y., & Tsuchiya, T. (2009). Unified analyses for *P-V-T* equation of state of MgO: A solution for pressure-scale problems in high *P-T* experiments. *Journal of Geophysical Research*, *114*, B03208. https://doi.org/10.1029/2008JB005813

Taylor, G. J. (2013). The bulk composition of Mars. *Chemie der Erde*, *73*(4), 401–420. https://doi.org/10.1016/j.chemer.2013.09.006

Terasaki, H., Nishida, K., Urakawa, S., Takubo, Y., Kuwabara, S., Shimoyama, Y., et al. (2019). Sound velocity and density of liquid $Ni_{68}S_{32}$ under pressure using ultrasonic and X-ray absorption with tomography methods. *Comptes Rendus Geoscience*, *351*(2-3), 163–170. https://doi.org/10.1016/j.crte.2018.04.005

Tsuchiya, T. (2003). First-principles prediction of the *P-V-T* equation of state of gold and the 660-km discontinuity in Earth's mantle. *Journal of Geophysical Research*, *108*(B10), B102463. https://doi.org/10.1029/2003JB002446

Urakawa, S., Kamuro, R., Suzuki, A., & Kikegawa, T. (2018). Phase relationships of the system Fe–Ni–S and structure of the high-pressure phase of $(Fe_{1-x}Ni_x)_3S_2$. *Physics of the Earth and Planetary Interiors*, *277*, 30–37. https://doi.org/10.1016/j.pepi.2018.01.007

Urakawa, S., Someya, K., Terasaki, H., Katsura, T., Yokoshi, S., Funakoshi, K., et al. (2004). Phase relationships and equations of state for FeS at high pressures and high temperatures and implications to the internal structure of Mars. *Physics of the Earth and Planetary Interiors*, *143-144*, 469–479. https://doi.org/10.1016/j.pepi.2003.12.015

Urakawa, S., Terasaki, H., Funakoshi, K., Uesugi, K., & Yamamoto, S. (2010). Development of high pressure apparatus for X-ray micro-tomography at SPring-8. *Journal of Physics Conference Series*, *215*, 012026. https://doi.org/10.1088/1742-6596/215/1/012026

Verhoeven, O., Rivoldini, A., Vacher, P., Mocquet, A., Choblet, G., Menvielle, M., et al. (2005). Interior structure of terrestrial planets: Modeling Mars' mantle and its electromagnetic, geodetic, and seismic properties. *Journal of Geophysical Research*, *110*, E04009. https://doi.org/10.1029/2004JE002271

Vinet, P., Rose, J. H., Ferrante, J., & Smith, J. R. (1989). Universal features of the equation of state of solids. *Journal of Physics. Condensed Matter*, *1*, 1941–1963. https://doi.org/10.1088/0953-8984/1/11/002

Wakabayashi, D., & Funamori, N. (2015). Solving the problem of inconsistency in the reported equations of state for h–BN. *High Pressure Research*, *35*(2), 123–129. https://doi.org/10.1080/08957959.2015.1028931

Wasson, J. T. (1989). The building stones of the planets. In F. Vilas, C. R. Chapman, & M. S. Matthews (Eds.), *Mercury*, (pp. 622–650). Tucson: University of Arizona Press.

Weber, R. C., Lin, P.-Y., Garnero, E. J., Williams, Q., & Lognonné, P. (2011). Seismic detection of the lunar core. *Science*, *331*(6015), 309–312 . https://doi.org/10.1126/science.1199375

Wieczorek, M. A., & Zuber, M. T. (2004). Thickness of the Martian crust: Improved constraints from geoid-to-topography ratios. *Journal of Geophysical Research*, *109*(E1), E01009. https://doi.org/10.1029/2003JE002153

Williams, J. G., Boggs, D. H., Yoder, C. F., Ratcliff, J. T., & Dickey, J. O. (2001). Lunar rotational dissipation in solid body and molten core. *Journal of Geophysical Research*, *106*(E11), 27,933–27,968. https://doi.org/10.1029/2000JE001396

Williams, J. G., Konopliv, A. S., Boggs, D. H., Park, R. S., Yuan, D. N., Lemoine, F. G., et al. (2014). Lunar interior properties from the GRAIL mission. *Journal of Geophysical Research: Space Physics*, *119*, 1546–1578. https://doi.org/10.1002/2013JE004559

Williams, Q., Manghnani, M. H., Secco, R. A., & Fu, S. (2015). Limitations on silicon in the outer core: Ultrasonic measurements at high temperatures and high d*K*/d*P* values of Fe-Ni-Si liquids at high pressures. *Journal of Geophysical Research: Solid Earth*, *120*, 6846–6855. https://doi.org/10.1002/2015JB012270

Yoder, C. F., Konopliv, A. S., Yuan, D. N., Standish, E. M., & Folkner, W. M. (2003). Fluid core size of Mars from detection of the solar tide. *Science*, *300*(5617), 299–303. https://doi.org/10.1126/science.1079645

Yu, X., & Secco, R. A. (2008). Equation of state of liquid Fe–17 wt%Si to 12GPa. *High Pressure Research*, *28*(1), 19–28. https://doi.org/10.1080/08957950701882138

Zharkov, V. N., & Gudkova, T. V. (2000). Interior structure models, Fe/Si ratio and parameters of figure for Mars. *Physics of the Earth and Planetary Interiors*, *117*(1-4), 407–420. https://doi.org/10.1016/S0031-9201(99)00110-7

Zharkov, V. N., & Gudkova, T. V. (2005). Construction of Martian interior model. *Solar System Research*, *39*(5), 343–373. https://doi.org/10.1007/s11208-005-0049-7